J. Fluid Mech. (1994), *vol.* 262, *pp.* 27–73

Observations of purely elastic instabilities in the Taylor–Dean flow of a Boger fluid

By YONG LAK JOO AND ERIC S. G. SHAQFEH
Department of Chemical Engineering, Stanford University, Stanford, CA 94305-5025, USA

(Received 2 February 1993 and in revised form 23 August 1993)

An experimental and theoretical investigation of the stability of the viscoelastic flow of a model Boger fluid between rotating cylinders with an applied pressure gradient is presented. In our theoretical study, a linear stability analysis based on the Oldroyd-B fluid model which predicts the critical conditions and the structure of the vortex flow at the onset of instability is developed. Our results reveal that certain non-axisymmetric modes are more unstable than the previously studied axisymmetric mode when the shearing by the cylinder rotation is the dominant flow-driving force. This is consistent with recent results presented by Beris & Avgousti (1992) on the stability of elastic Taylor–Couette flow. On the other hand, the axisymmetric mode is more unstable when the pressure gradient becomes dominant. Furthermore, we investigate the mechanism of purely elastic Taylor–Dean instability with respect to non-axisymmetric disturbances through an examination of the disturbance-energy equation. It is found that the mechanism of the elastic Taylor–Dean instability is associated with the coupling between the disturbance polymeric stresses due to the azimuthal variation of the disturbance flow and the base state velocity gradients. In our experimental study, evidence of non-inertial, cellular instabilities in the Taylor–Dean flow of a well-characterized polyisobutylene/polybutene Boger fluid is presented. A stationary, meridional obstruction is placed between independently rotating, concentric cylinders to generate an azimuthal pressure gradient in opposition to the shearing flow. Flow visualization experiments near the critical conditions show the transition from purely azimuthal flows to secondary vortex flows, and the development of evenly spaced, banded vortex structures. The critical wavenumber obtained from spectral image analysis of the visualizations, and the critical Deborah number are presented for various ratios of the pressure gradient to the shear driving force. Although there is a quantitative discrepancy between data and theory, the qualitative trends in the data are in agreement with our theoretical predictions. In addition, laser-Doppler velocimetry (LDV) measurements show that the instability is a stationary mode when the pressure gradient is the dominant flow-driving force, while it is an oscillatory instability when the shearing is dominant, again as predicted by the theory.

1. Introduction

The stability of the viscous flow between concentric cylinders was first investigated experimentally and theoretically by Taylor (1923). He showed, in agreement with experiment, that a secondary motion in the form of toroidal vortices occurs when the parameter $Re(d/R_1)^{\frac{1}{2}}$ exceeds a value of about 41, where d is the spacing between the cylinders, R_1 is the radius of the inner cylinder, and Re is the Reynolds number for the flow in the gap. Taylor assumed both that $d/R_1 \ll 1$, and that the disturbance flow is azimuthally symmetric, however, he did observe non-axisymmetric flows in some of his experiments. To be specific, he noted that as the Reynolds number is increased, the axisymmetric Taylor vortices become unstable, and a new flow is established which is characterized by travelling azimuthal waves superimposed on the Taylor vortices. The linear stability of Taylor–Couette flow with respect to non-axisymmetric disturbances was studied by DiPrima (1961). He found that the critical value of the Reynolds number increased with the azimuthal wavenumber, but that non-axisymmetric disturbances are only slightly more stable than axisymmetric ones. This wavy instability was studied experimentally by Coles (1965). Higher transitions, which occur as the Reynolds number is increased beyond the critical value, are discussed in the review by DiPrima & Swinney (1981).

A similar instability occurs in the viscous flow through a curved channel when driven by a streamwise pressure gradient. This instability was first studied by Dean (1928) for a channel formed by two concentric cylinders, again under the assumptions that the spacing d between the cylinders was small relative to the radius of the inner cylinder R_1 and that the disturbance flow was azimuthally symmetric. He found that flow instability first occurs when $Re(d/R_1)^{\frac{1}{2}}$ exceeds a value of about 36, where Re is the Reynolds number based on the mean velocity of the unperturbed flow. When rotation and an azimuthal pressure gradient are both present, the instability of this Taylor–Dean flow has some distinctive features which are absent from either limiting case. The latter problem was first studied experimentally by Brewster & Nissan (1958), while DiPrima analysed theoretically the case where the inner cylinder rotates and the flow is simultaneously driven by a uniform circumferential pressure gradient. Raney & Chang (1971) investigated the stability of Taylor–Dean flow to non-axisymmetric disturbances. Their theoretical analysis shows that some non-axisymmetric, oscillatory modes can be more unstable than the axisymmetric mode in certain flow parameter regimes. This was verified experimentally by Mutabazi *et al.* (1989, 1990) using a device where corotating cylinders mounted horizontally were used to generate Taylor–Dean flows by only partially filling the gap with liquid.

For non-Newtonian fluids, instabilities may arise when the Deborah number, De, which represents the importance of elastic forces in the flow, reaches a critical magnitude (e.g. Phan-Thien 1983, 1985; Larson, Shaqfeh & Muller 1990; Joo & Shaqfeh 1991, 1992). Under many circumstances inertial instabilities or bifurcations are unimportant because the relevant Reynolds numbers are very small. Larson *et al.* (1990) predict a purely elastic instability in the Taylor–Couette flow of an Oldroyd-B fluid from a linear stability analysis considering only axisymmetric flows. They have found that the instability is time-periodic and experiments show the existence of a non-inertial cellular instability. Joo & Shaqfeh (1991, 1992) reported the discovery of a new purely elastic instability in the pressure-driven Dean flow of an elastic fluid through a curved channel as predicted through an analysis of the flow of an Oldroyd-B model fluid. The instability mode was found to be stationary in contrast to the elastic, oscillatory instability in Taylor–Couette flow. Again, only axisymmetric instability modes were considered by these co-workers. In addition, the mechanism of both the purely elastic stationary and oscillatory instabilities in Dean and Taylor–Couette flow have been examined elsewhere (Larson *et al.* 1990; Joo & Shaqfeh 1992). It is found that the instability mechanism of the Dean flow, where the instability is a stationary mode, is associated with the coupling of the perturbation velocity field to the polymeric normal stress gradients in the base flow (Joo & Shaqfeh 1992). In contrast, the mechanism for the elastic, oscillatory instability in Taylor–Couette flow involves the coupling between the disturbance polymeric stresses and the base state velocity gradients (Larson *et al.* 1990).

A purely elastic instability in Taylor–Dean flow which combines cylinder rotation and a pressure gradient as flow-driving forces in flow through a curved channel was also reported by Joo & Shaqfeh (1992). The linear stability results reveal that the instability is a stationary mode when the pressure gradient becomes the dominant flow-driving force, while it is an oscillatory instability when the shearing by the cylinder rotation is dominant. In addition, it is found that the direction of the pressure gradient controls the characteristics of the instability: a pressure gradient applied along the cylinder rotation destabilizes the flow, while if applied against the rotation, the flow is substantially stabilized.

As mentioned above, in these previous studies (Larson *et al.* 1990; Joo & Shaqfeh 1991, 1992) of the purely elastic instabilities in Taylor–Couette and Taylor–Dean flows, only axisymmetric disturbance flows are considered. Although the experiments in Taylor–Couette flow by Larson *et al.* (1992) show the existence of a non-inertial secondary flow, their theoretical analysis including only axisymmetric disturbances overpredicts the critical Deborah number. Recently, Beris & Avgousti (1992) have reported that non-axisymmetric disturbances are more unstable than the axisymmetric disturbances in the viscoelastic Taylor–Couette flow of a Maxwell fluid.

The purpose of the present communication is twofold. First, we examine the purely elastic instability in the Taylor–Dean flow of an Oldroyd-B fluid model with respect to non-axisymmetric disturbances. The critical conditions and the structure of the vortex flow at the onset of the instability for a complete series of Taylor–Dean flows from Taylor–Couette flow (shear dominant flow) to Dean flow (pressure dominant flow) are presented. Our results reveal that certain non-axisymmetric modes are more unstable than the axisymmetric mode when the shearing by the cylinder rotation is the dominant flow-driving force, while the axisymmetric mode is more unstable when the pressure gradient becomes dominant. Furthermore, we investigate the mechanism of purely elastic Taylor–Dean instability with respect to non-axisymmetric disturbances through an examination of the disturbance-energy equation. A new mechanism of the instability is uncovered: when the disturbances are non-axisymmetric, it is found that the mechanism of the elastic Taylor–Dean instability is associated with the coupling between the disturbance polymeric stresses due to the azimuthal variation of the disturbance flow and the base state velocity gradients. This coupling which arises from the coupling of the azimuthal variation of the radial perturbation velocity to the azimuthal normal stress in the base state is absent when the disturbances flows are axisymmetric. In addition, we relax the small-gap assumption and examine finite-gap effects on the stability of elastic Taylor–Dean flows. It is demonstrated that all flows are stabilized by finite-gap effects. Calculations for Taylor–Couette flow are presented for the gap ratios in the range $0 < d/R_1 \leqslant 0.35$. These are then compared with the previous experimental results by Larson *et al.* (1990) and Shaqfeh, Muller & Larson (1992). The effects of the gap width in Dean flow are also presented.

After examining the linear stability of Taylor–Dean flow with respect to non-axisymmetric disturbances, we turn to the second purpose of this communication in which an experimental investigation of non-inertial, cellular instabilities in the Taylor–Dean flow of a well-characterized polyisobutylene/polybutene Boger fluid is presented. A stationary, meridional obstruction is placed between independently rotating, concentric cylinders to generate an azimuthal pressure gradient in opposition to the shearing flow. By changing the ratio of the rotation rate of the inner cylinder to the outer cylinder, a complete series of Taylor–Dean flows are examined. Flow-visualization experiments near the critical conditions show the transition from purely azimuthal flows to secondary vortex flows, and the development of evenly spaced,

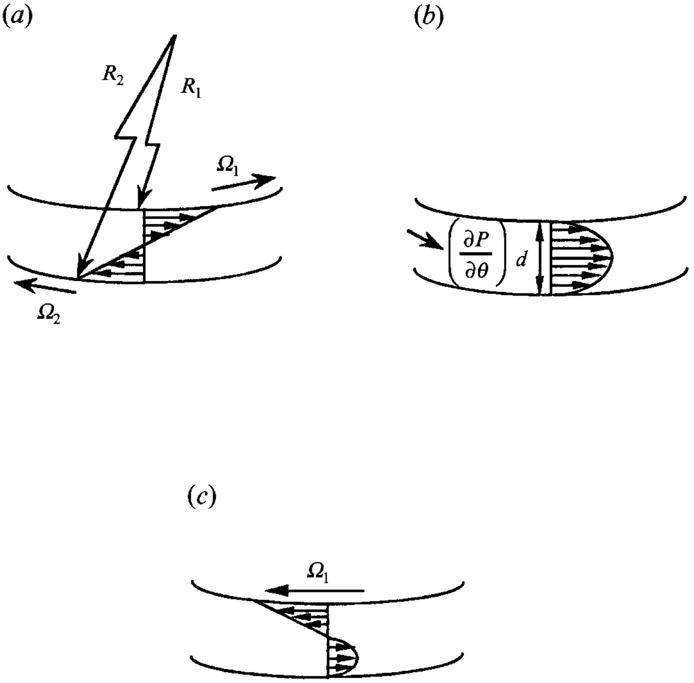

FIGURE 1. Flow driving forces in (*a*) Taylor–Couette flow (cylinder rotation), (*b*) Dean flow (an azimuthal pressure gradient), and (*c*) Taylor–Dean flow (cylinder rotation and an azimuthal pressure gradient).

banded vortex structures. The critical wavenumber obtained from spectral image analysis, and the critical Deborah number are presented for various ratios of the pressure gradient to the shear driving force. Although there is a quantitative discrepancy between data and theory, the qualitative trends in the data are in agreement with our theoretical predictions. Finally, laser-Doppler velocimetry (LDV) measurements show that the instability is a stationary mode when the pressure gradient becomes the dominant flow-driving force, while it is an oscillatory instability when the shearing is dominant as predicted by the theory.

2. Theory

2.1. *Development of the linear stability equations*

We consider the flow of a fluid between two concentric cylindrical surfaces. The flow is driven by the rotation of the cylindrical surfaces or a constant pressure gradient acting around the cylinders or both (see figure 1).

The linear growth of the disturbance can be determined from linear stability equations derivable from the continuity, momentum conservation and a suitable constitutive equation. We choose the Oldroyd-B constitutive equation because of its usefulness in describing the flow behaviour of even highly elastic flows. The Oldroyd-B model can be derived from a molecular theory in which the polymer molecules are modelled as non-interacting Hookean elastic dumb-bells immersed in a Newtonian solvent (see Bird *et al.* 1987). It has previously been shown that the Oldroyd-B constitutive equation provides a useful description of the rheological behaviour of dilute polymer solutions in shearing flow over a range of shear rate (e.g. Boger 1977/1978; Gupta, Sridhar & Ryan 1983; Mackay & Boger 1987). We also note that

Quinzani *et al.* (1991) have discussed the rheology of Boger fluids in great detail and have remarked on the limitations of characterizing the fluid rheology with a multimode Oldroyd-B model. We apply the same methodology as discussed in our previous publication (Joo & Shaqfeh 1992) where a detailed development of the linear stability equations for axisymmetric disturbances can be found.

Since we shall show that not only the ratio of the applied pressure gradient to the shear driving force but also the direction of these two driving forces control the characteristics of the instability, we shall distinguish between the following two cases: a flow where the shear rate due to the rotation of the cylinders is positive ($\beta = (\Omega_2 - \Omega_1)/\Omega_1 > 0$ where Ω_1 and Ω_2 are the rotation rates of the inner and outer cylinder, respectively, see figure 1), and a flow where it is negative ($\beta < 0$). In both cases, we assume the direction of the azimuthal pressure gradient is positive, i.e. $\partial P/\partial\theta > 0$, where θ denotes an azimuthal coordinate. In §4.2 we present a Taylor–Dean flow apparatus which generates a positive pressure gradient, and changing the ratio of the rotation rate of the inner cylinder to the outer cylinder can alter not only the shear rate due to the shearing force but also the magnitude of the pressure gradient. In this section, we shall restrict our discussion to the case when the gap $d = R_2 - R_1$ is small compared to either R_1 or R_2, i.e. $\varepsilon = d/R_1 \ll 1$. The effects of finite gap will be presented in §3.

With Cauchy's equations of motion, the Oldroyd-B constitutive equation, and the boundary conditions, the velocity distribution describing the basic flow for $\varepsilon \ll 1$ can be written as the sum of two terms: a simple shearing flow due to the cylinder rotation, and a Poiseuille flow due to the azimuthal pressure gradient, namely (see Joo & Shaqfeh (1992),

$$v_\theta^0 \approx v_y^0 = \Omega_1 R_1 \left(\xi(x - x^2) + \left(\frac{\Omega_1}{|\Omega_1|} + \beta x \right) \right), \tag{1}$$

where $\xi = -(\partial P/\partial\theta)\, d^2/2\eta_t R_1^2 \Omega_1$ represents the relative importance of the pressure gradient to the cylinder rotation as a flow driving force, and η_t is the shear viscosity. In addition, $x = (r - R_1)/(R_2 - R_1)$ is the gap variable, and y denotes a streamwise direction or azimuthal coordinate.

For $\beta > 0$, we have from (1) the following approximate dimensionless expression for the velocity gradient (made dimensionless with the product of the gap d and the maximum shear rate across the gap, $\dot\gamma_{max} = (\Omega_1 d/R_1)(-\xi + \beta)$):

$$v_y^{0\prime} = -\delta(1 - 2x) + (1 - \delta), \tag{2}$$

where $\delta = \xi/(\xi - \beta)$, and the prime refers to a derivative with respect to the gap variable x.

For $\beta < 0$, we have a similar expression for the velocity gradient (made dimensionless with the product of the gap d and the maximum shear rate, $\dot\gamma_{max} = (\Omega_1 d/R_1)(-\xi - \beta)$):

$$v_y^{0\prime} = -\delta^*(1 - 2x) + (\delta^* - 1), \tag{3}$$

where δ^*, which is analogous to δ, is defined as $\xi/(\xi + \beta)$.

For both cases, we have the following expressions for the stress fields (see Joo & Shaqfeh 1991) again for $\varepsilon \ll 1$:

$$\tau_{r\theta}^0 \approx \tau_{xy}^0 = v_y^{0\prime}, \tag{4}$$

$$\tau_{\theta\theta}^0 \approx \tau_{yy}^0 = 2De(1 - S)(v_y^{0\prime})^2, \tag{5}$$

where S is the ratio of solvent to total shear viscosity, i.e. η_s/η_t. In (4)–(5), the stresses are made dimensionless with a characteristic stress chosen as the product of the shear viscosity and the maximum shear rate across the gap, $\eta_t \dot\gamma_{max}$. The Deborah number in

(4) is defined as the product of the fluid relaxation time λ and the maximum shear rate, $\dot{\gamma}_{max}$:

$$De = \frac{\Omega_1}{\varepsilon}(-\xi+\beta)\,\lambda \quad \text{for } \beta > 0, \tag{6}$$

$$De = \frac{\Omega_1}{\varepsilon}(-\xi-\beta)\,\lambda \quad \text{and for } \beta < 0. \tag{7}$$

For the limiting cases, $\delta = \delta^* = 0$ and $\delta = \delta^* = 1$, (2)–(5) become the expressions for the velocity and stress fields for Taylor–Couette flow and Dean flow, respectively (Joo & Shaqfeh 1992).

We then consider the evolution of small normal mode disturbances applied to these base states. For general (i.e. axisymmetric and non-axisymmetric) disturbances, the velocities and stresses become

$$\boldsymbol{v} = (0, v_\theta^0, 0) + (U(r), V(r), W(r))\exp(\mathrm{i}(\sigma z + n\theta - \omega t)), \tag{8}$$

$$\tau = \begin{pmatrix} 0 & \tau_{r\theta}^0 & 0 \\ \tau_{r\theta}^0 & \tau_{\theta\theta}^0 & 0 \\ 0 & 0 & 0 \end{pmatrix} + \begin{pmatrix} RR(r) & R\theta(r) & RZ(r) \\ R\theta(r) & \theta\theta(r) & \theta Z(r) \\ RZ(r) & \theta Z(r) & ZZ(r) \end{pmatrix} \exp(\mathrm{i}(\sigma z + n\theta - \omega t)). \tag{9}$$

We shall be considering the temporal stability of the flow, so ω is in general a complex frequency and σ is the real axial wavenumber. Thus, this formulation allows for the consideration of overstable as well as stationary modes. In (8) and (9), n is the azimuthal wavenumber, which is an integer (positive, negative, or zero) owing to the periodicity in a Couette geometry. For the laboratory simulation of the Taylor–Dean flow, the flow regime is separated by a block (see figure 12). Under these conditions, the perturbations need not be periodic in the azimuthal direction, and one needs to solve for a general class of non-axisymmetric perturbations which satisfy the requisite boundary conditions in θ. However, we shall consider only periodic disturbances in our analysis, realizing that these do not exactly model our experimental conditions. Note that only periodic disturbances have been considered in the analysis of inertial Taylor–Dean instabilities by Raney & Chang (1971). It follows from (8) and (9) tht the disturbances become axisymmetric, if $n = 0$.

Substitution of the disturbances (8) and (9) into Cauchy's equations of motion, the Oldroyd-B constitutive equation, and the continuity equation, followed by linearization allows us to derive a set of linear stability equations. Setting the Reynolds number equal to zero in order to examine only elastically driven instabilities, and simplifying, these equations can then be reduced to an eigenvalue problem for the complex frequency $\bar{\omega}$ (made dimensionless with the characteristic relaxation time λ):

$$\begin{aligned} U'''' - 2\alpha^2 U'' + \alpha^4 U &+ \frac{2\alpha^2 \varepsilon De^2 \mathscr{D}(1-S)\, v_y^{0'}}{S+\mathscr{D}(1-S)}[\mathscr{D}(1+2\mathscr{D})\, v_y^{0'}\, U' - (2+\mathscr{D})\, v_y^{0''}\, U] \\ &+ \frac{4\mathrm{i}n\alpha^2\varepsilon^2 De^3 \mathscr{D} e^2 (1+D)(1-S)}{S+\mathscr{D}(1-S)}(v_y^{0'})^3\, U + \frac{2\alpha^2 \varepsilon De \mathscr{D}(1+\mathscr{D})(1-S)}{S+\mathscr{D}(1-S)}\, v_y^{0'}\, V' \\ &+ \frac{2\mathrm{i}n\alpha^2\varepsilon^2 De^2 \mathscr{D}(2+\mathscr{D})(1-S)}{S+\mathscr{D}(1-S)}(v_y^{0'})^2\, V = 0, \end{aligned} \tag{10}$$

$$\begin{aligned} V'' - \alpha^2 V &+ \frac{De\, \mathscr{D}^2(1-S)}{S+\mathscr{D}(1-S)}(v_y^{0'}\, U'' + 2v_y^{0''}\, U' - \alpha^2 v_y^{0'}\, U) - \frac{2n^2\varepsilon^2 De^3 \mathscr{D}(1-S)}{S+\mathscr{D}(1-S)}(v_y^{0'})^3\, U \\ &+ \frac{\mathrm{i}n\varepsilon De^2\, \mathscr{D}^2(1-S)}{S+\mathscr{D}(1-S)}[2(v_y^{0'})^2\, U' + 3v_y^{0'}\, v_y^{0''}\, U] \\ &- \frac{\mathrm{i}n\varepsilon De\, \mathscr{D}(1-S)}{S+\mathscr{D}(1-S)}[2v_y^{0'}\, V' + v_y^{0''}\, V] = 0, \end{aligned} \tag{11}$$

with the boundary conditions:

$$V = U = U' = 0 \quad \text{at} \quad x = 0, \quad x = 1. \tag{12}$$

In (10)–(11) α is the axial wavenumber of the disturbance made dimensionless with the gap, and $\mathscr{D} = 1/(1-\mathrm{i}\bar{\omega}+\varepsilon \mathrm{i} n De\, v_y^0)$. Note that (10) and (11) constitute the small-gap eigenvalue problem in the sense that we have retained terms of $O(\varepsilon^2 De^3)$ and larger, keeping in mind that $De \sim O(\varepsilon^{-\frac{1}{2}})$, when $\varepsilon \ll 1$ for instability. Strictly speaking then, terms of $O(\varepsilon^2 De^3)$ are small like $O(\varepsilon^{\frac{1}{2}})$ and in the limit $\varepsilon \to 0$ but $\varepsilon^{\frac{1}{2}} De \sim O(1)$ all modes have the same stability characteristics (i.e. critical De and α) as reported by Joo & Shaqfeh (1992) and given by (14) and (15). However, we find that for any reasonable gap size ($\varepsilon > 10^{-4}$) the terms of $O(\varepsilon^2 De^3)$ are important. In addition, only these terms distinguish the stability of modes with different azimuthal symmetry, i.e. different values of n. This will be demonstrated in our numerical results in §3. For a detailed derivation of (10)–(11) reference should be made elsewhere (see Joo 1993).

For the axisymmetric modes, (11) and the boundary conditions (12) imply that

$$V = -\frac{\mathscr{D}^2 De(1-S)}{S+\mathscr{D}(1-S)} v_y' \, U. \tag{13}$$

This result allows us to eliminate V from (10). Thus, we recover the eigenvalue problem governing the linear growth of small axisymmetric disturbances for Taylor–Dean flow in the narrow gap limit (see Joo & Shaqfeh 1992)

$$U'''' - 2\alpha^2 U'' + \alpha^4 U + \varepsilon De^2 \alpha^2 \Lambda_1(\bar{\omega}) (v_y^{0'})^2 U' - \varepsilon De^2 \alpha^2 \Lambda_2(\bar{\omega}) v_y^{0'} v_y^{0''} U = 0, \tag{14}$$

together with the boundary conditions

$$U = U' = 0 \quad \text{at} \quad x = 0, \quad x = 1. \tag{15}$$

In (14), Λ_1 and Λ_2 are related to the important dimensionless variables via the expressions

$$\Lambda_1 = 2\mathscr{D}^2(1-S)\left[\frac{1+2\mathscr{D}}{S+\mathscr{D}(1-S)} - \frac{\mathscr{D}(1+\mathscr{D})(1-S)}{S+\mathscr{D}(1-S)^2}\right], \tag{16}$$

$$\Lambda_2 = 2\mathscr{D}(1-S)\left[\frac{2+\mathscr{D}}{S+\mathscr{D}(1-S)} + \frac{\mathscr{D}(1+\mathscr{D})(1-S)}{S+\mathscr{D}(1-S)^2}\right]. \tag{17}$$

2.2. *Neutral stability curves*

An orthogonal shooting solution method was employed to explicitly solve the eigenvalue problem (10)–(12). This method has been applied to other stability problems and for details reference should be made to the appropriate publications (Keller 1961; Conte 1966; Shaqfeh & Acrivos 1987). In this scheme, a standard fourth-order Runge–Kutta integrator with constant step size was used, and a complex secant method was employed to iterate and obtain convergence on the eigenvalue. Note that in the present application, it was found that the eigenvalue problem is fairly stiff and that at least two orthonormalizations are required to retain five-digit numerical accuracy in the solutions during integration with the step size 0.01. The number of orthonormalizations increases as either axial or azimuthal wavenumber of the eigenmode increases. For some cases ($0.4 \leqslant \delta^* \leqslant 0.6$), the eigenvalue problem was found to be extremely stiff owing to the large values of the axial wavenumber and the Deborah number near the stability boundary, and thus the five-digit accuracy

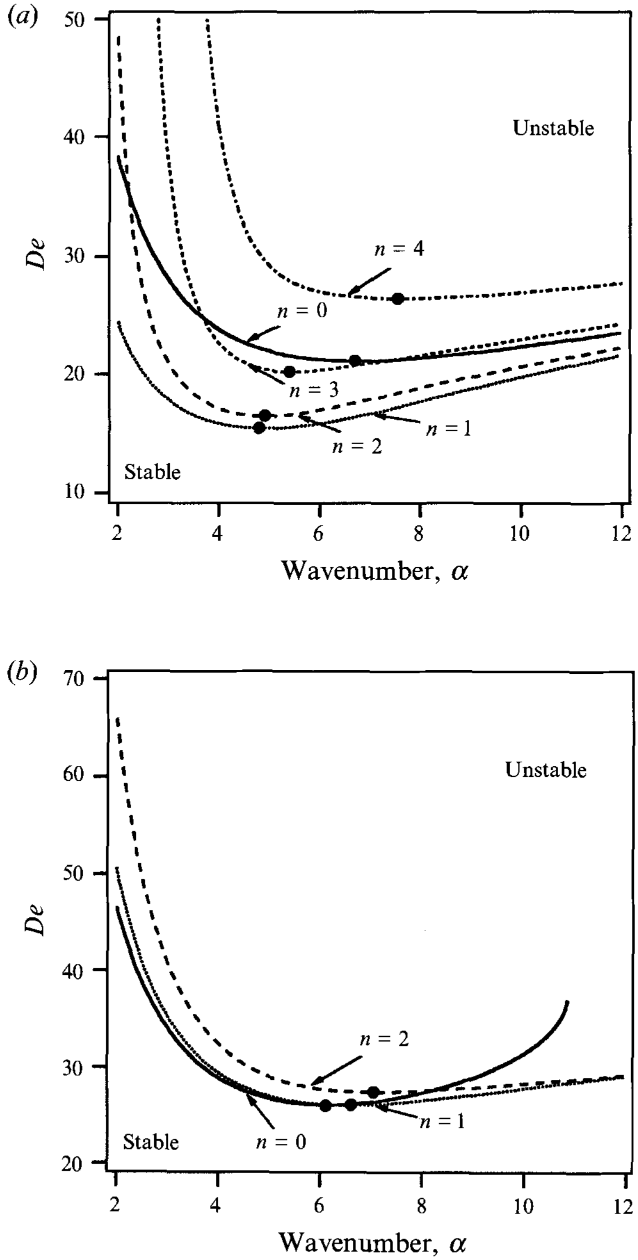

FIGURE 2. Neutral curves De_{cr} *vs.* α for (*a*) Taylor–Couette flow, and (*b*) Dean flow. The calculations for both axisymmetric ($n = 0$) and non-axisymmetric ($n = 1$, $n = 2$, $n = 3$ and $n = 4$) modes are shown.

mentioned above was not obtained even with increasing orthonormalizations and reducing the integration step size. For obtaining precise values of the critical conditions under this very limited range of conditions, one must either use an alternative numerical method or employ a large wavenumber analysis. We also scanned the complex frequency domain at the critical wavenumber and Deborah number to determine the set of eigenmodes and eigenvalues for all Taylor–Dean instabilities (Joo 1993). By this mode-scanning procedure, we can also determine the most unstable

β	$n = 0$	$n = 1$	$n = 2$	$n = 3$	$n = 4$
-1	± 0.779	0.100	0.632	1.210	1.570
-2	± 0.779	-0.936	-1.564	-2.843	-5.506
∞	± 0.779	1.968	3.753	6.890	12.58

TABLE 1. Frequency of oscillation in the unstable modes of Taylor–Couette flow for various azimuthal wavenumbers

mode and further understand the structure of these eigenvalue problems (see Joo & Shaqfeh 1992; Joo 1993). Below, we present the characteristics of the purely elastic instability with respect to non-axisymmetric disturbances in Taylor–Dean flow. This includes the neutral stability curves and the vortex structure at the onset of instability.

In our previous publication (Joo & Shaqfeh 1992), we presented the characteristics of the instability with respect to axisymmetric disturbances in Taylor–Dean flow. We found that a pressure gradient applied along the cylinder rotation destabilizes the flow, while if applied against the cylinder rotation, the flow is substantially stabilized. In this section, we shall compare these previous results for axisymmetric disturbances with the present results for non-axisymmetric disturbances. In what follows, the ratio of solvent to total viscosity S and the dimensionless gap ε are chosen to represent our experimental conditions, 0.8 and 0.13, respectively (see §4). The effects of gap width and solvent ratio will be discussed in §3. First, we present the neutral curves for the limiting cases, Taylor–Couette flow ($\delta = \delta^* = 0$) and Dean flow ($\delta = \delta^* = 1$). In figure 2(*a*), we plot the neutral curves, *De vs.* α, for the purely elastic Taylor–Couette flow at various values of the azimuthal wavenumber n. In the region below each curve, the corresponding mode is stable, while it is unstable in the region above. It is observed that the critical values of the Deborah number (shown with the symbols ● in figure 2*a*) decrease first, and then increase as the azimuthal number n is increased. Thus, the non-axisymmetric modes, $n = 1$, $n = 2$, and $n = 3$ are the more unstable than the axisymmetric mode ($n = 0$), and the non-axisymmetric mode with $n = 1$ is the most unstable one. Note that for Taylor–Couette flow in the small-gap limit, both axisymmetric and non-axisymmetric modes are oscillatory, and that the critical Deborah number and the critical wavenumber of each mode do not depend on the relative rotation rate between inner and outer cylinders β. However, it is found that the frequency of oscillation of the non-axisymmetric modes depend on β, while that of the axisymmetric mode does not depend on β as shown in table 1. Furthermore, the frequency for the non-axisymmetric modes monotonically increases as wavenumber is increased. For two Taylor–Couette flows at different values of β we have the same eigenvalue $\mathscr{D}$, since the azimuthal velocity in the base state (v_y^0) appears in the final eigenvalue problem (10)–(12) only via $\mathscr{D} = 1/(1-\mathrm{i}\bar{\omega}+\varepsilon \mathrm{i} n De v_y^0)$. Therefore, the critical Deborah number and the critical wavenumber for Taylor–Couette flow do not depend on the relative rotation rate β, and the two frequencies of oscillation for Taylor–Couette flows at two different values of β have the following relation:

$$\bar{\omega}_1 - \bar{\omega}_2 = n\varepsilon De[(v_y^0)_1 - (v_y^0)_2]. \tag{18}$$

This result will be used to examine the nature of the instability in §5. Finally, we note that the critical wavenumber α_c decreases first, and then increases as the azimuthal wavenumber n is increased.

We have also plotted neutral curves for Dean flow at various values of the azimuthal wavenumber in figure 2*b*. It is observed that the critical Deborah number increases as

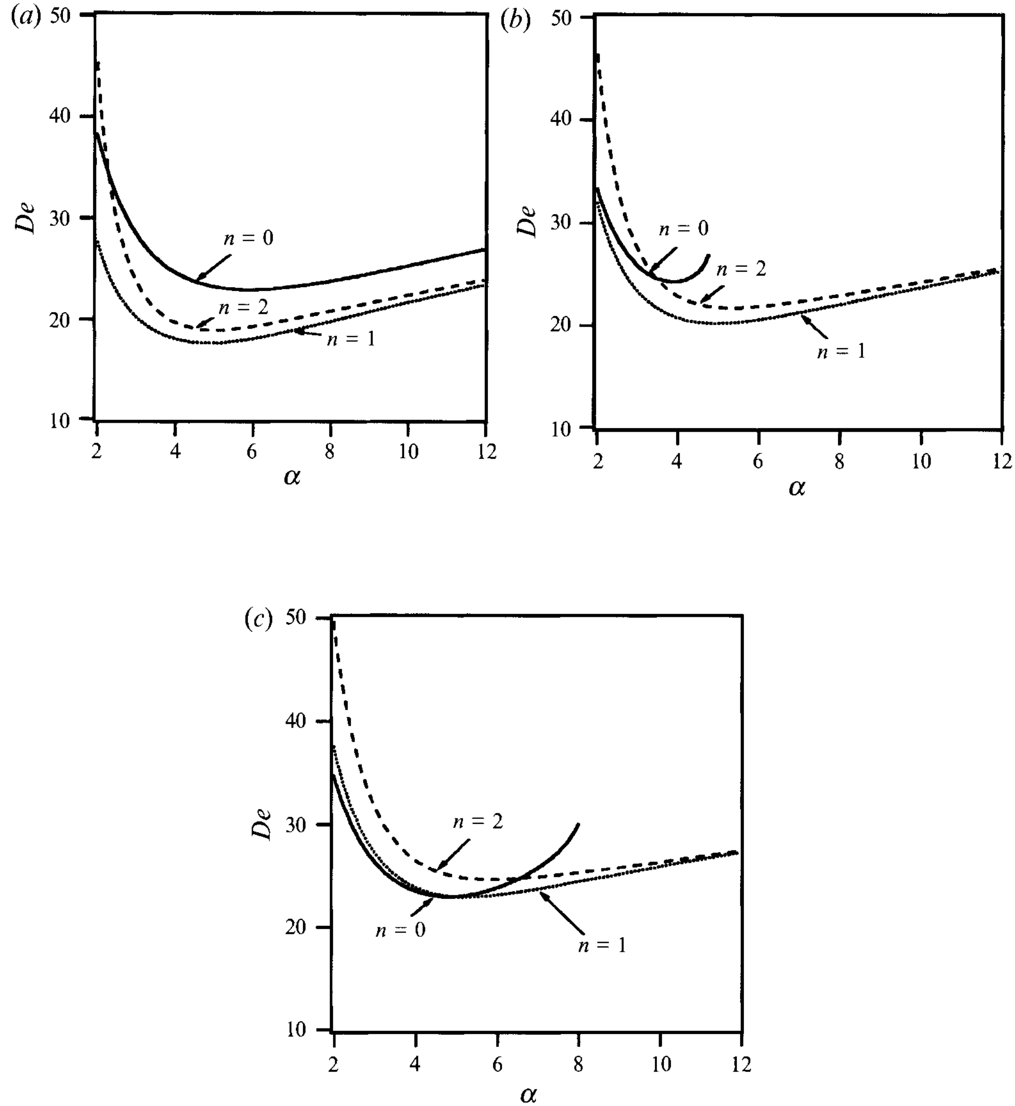

Figure 3. Neutral curves for Taylor–Dean flows when the velocity gradient due to the shearing by the cylinder rotation is positive ($\beta > 0$): (a) $\delta = 0.25$, (b) $\delta = 0.5$, (c) $\delta = 0.75$.

the azimuthal wavenumber n is increased. This indicates that the axisymmetric mode ($n = 0$) is more unstable than any non-axisymmetric mode. The neutral stability curves for integer values of the azimuthal wavenumber are shown figure 2b. It is also observed that the critical wavenumber monotonically increases as the azimuthal wavenumber is increased. Note that for Dean flow, the axisymmetric mode is a stationary one, while the non-axisymmetric modes are oscillatory.

Neutral curves for Taylor–Dean flow at three different values of δ are shown in figure 3, when the shear rate due to the rotation of the cylinders is positive ($\beta > 0$). It is observed that when the shearing by the cylinder rotation is the dominant flow driving force ($\delta = 0.25$, figure 3a), the stability characteristics are similar to those of Taylor–Couette flow: the critical Deborah number decreases first, and then increases as the azimuthal wavenumber n is increased. It is also observed that the critical

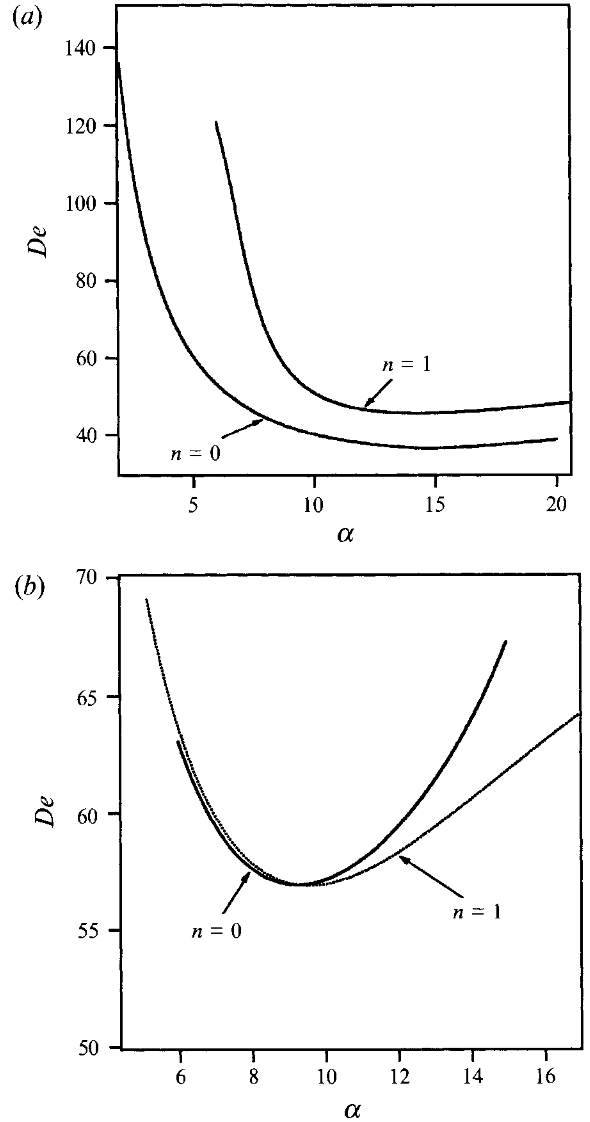

FIGURE 4. Neutral curves for Taylor–Dean flows when the velocity gradient due to the shearing by the cylinder rotation is negative ($\beta < 0$): (a) $\delta^* = 0.25$, (b) $\delta^* = 0.75$.

wavenumber decreases as the azimuthal wavenumber is increased. On the other hand, the stability characteristics are similar to those of Dean flow, when the pressure gradient is dominant ($\delta = 0.75$, figure 3c): both the critical Deborah number and the critical wavenumber increase as the azimuthal wavenumber is increased. When both flow-driving forces are comparable ($\delta = 0.5$, figure 3b), the critical Deborah number decreases first, and then increases, but the critical wavenumber only increases, as the azimuthal wavenumber is increased. In general, the critical Deborah number monotonically increases as δ is increased, and thus the applied pressure gradient stabilizes the flow.

In figure 4, we plot neutral curves for Taylor–Dean flow at two different values of δ^*, when the shear rate due to the rotation of the cylinders is negative ($\beta < 0$). It is shown that the non-axisymmetric mode is more unstable than the axisymmetric one

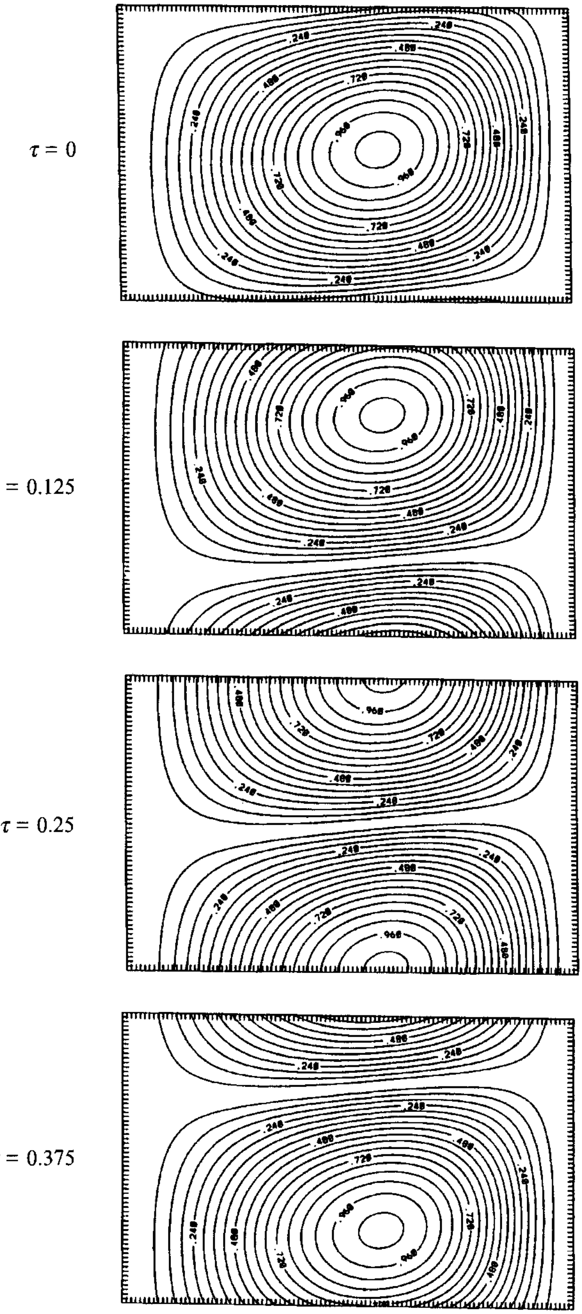

FIGURE 5. Time sequences of a possible travelling wave pattern at the onset of Taylor–Couette flow at $S = 0.8$, $\varepsilon = 0.133$, $\beta = -1$, $n = 1$, $\theta = 0$.

when the shearing is the dominant flow-driving force ($\delta^* = 0.25$, figure 4*a*), while the axisymmetric mode is more unstable when the pressure gradient becomes dominant ($\delta^* = 0.75$, figure 4*b*). Note that the critical Deborah number substantially increases first, and then decreases as δ^* increased. The critical wavenumber and the critical Deborah number obtained from flow-visualization experiments will be compared with these theoretical predictions in §5.

2.3. *Streamlines at the onset of instability*

In this section we examine the possible secondary vortex flow structures which are predicted from the linear analysis at the onset of the instability. The complex stream function corresponding to the non-axisymmetric disturbance flow in the (x, z)-plane is defined

$$\Psi = \psi(x) \exp \mathrm{i}(\alpha z + n\theta - \omega t), \tag{19}$$

where $\psi = \mathrm{i}\, U/\alpha$.The real stream function of the growing mode which moves 'up' the coaxial cylinders becomes

$$\Psi_r^{0(1)} = -\frac{1}{\alpha}\{U_i \cos[2\pi(Z + n\theta - \Gamma)] + U_r \sin[2\pi(Z + n\theta - \Gamma)]\}. \tag{20}$$

In (20), we have rescaled the Z-coordinate and time, Γ, with the wavelength of the critical disturbance and the period of its oscillation, respectively. In figure 5, we have plotted time sequences of this possible travelling 'spiral' wave pattern for Taylor–Couette flow at $\theta = 0$. The left boundary of the graph represents the inner cylinder, and the right is the outer cylinder. As we can see in (20), there is equivalence between azimuthal variation (θ) and time variation (Γ) in the vortex structure, and thus for $n = 1$ the four time sequences of the spirals at $\theta = 0$ shown in figure 5 are identical to the vortex structures at the four different azimuthal positions ($\theta = 0$, $\theta = 45°$, $\theta = 90°$, and $\theta = 135°$, respectively) at $\Gamma = 0$. Meanwhile, there can be an equivalent mirror-image structure that moves spirally 'down' the coaxial cylinders, and the real stream function of this mode are:

$$\Psi_r^{0(2)} = -\frac{1}{\alpha}\{-U_i \cos[2\pi(Z - n\theta + \Gamma)] + U_r \sin[2\pi(Z - n\theta + \Gamma)]\}. \tag{21}$$

Although nonlinear analysis is necessary to determine whether travelling 'spirals' or standing 'ribbons' (formed from the superposition of two counter-travelling spirals) are chosen, the real stream function for the standing wave pattern can be written as the sum of two stream functions, (20) and (21):

$$\begin{aligned}\Psi_r^{0} = -\frac{1}{\alpha}\{&U_i \cos[2\pi(Z + n\theta - \Gamma)] + U_r \sin[2\pi(Z + n\theta - \Gamma)] \\ &- U_i \cos[2\pi(Z - n\theta + \Gamma)] + U_r \sin[2\pi(Z - n\theta + \Gamma)]\}.\end{aligned} \tag{22}$$

Time sequences of the standing wave pattern in the (x, z)-plane for the axisymmetric mode ($n = 0$) and for the non-axisymmetric mode ($n = 1$) in Taylor–Couette flow at $\theta = 0$ are shown in figure 6. Since the critical wavenumber of the non-axisymmetric mode is smaller than that of the axisymmetric mode, the axial dimension of the vortex structure for the former is larger. It is shown that for the non-axisymmetric mode, the vortex is located near the outer cylinder, while it is symmetric about the centre of the gap for the axisymmetric mode. Again, owing to the equivalence between the azimuthal variation (θ) and the time variation (Γ) in the vortex structure, the four time sequences of the ribbons at $\theta = 0$ shown in figure 6(*b*) are identical to the vortex structures at four different azimuthal positions ($\theta = 0$, $\theta = 45°$, $\theta = 90°$, and $\theta = 135°$, respectively) at $\Gamma = 0$. Finally, we note that although these streamlines are for Taylor–Couette flow, no qualitative changes in the structures of the oscillatory non-axisymmetric mode were found in Taylor–Dean flow (see Joo 1993). The structures of

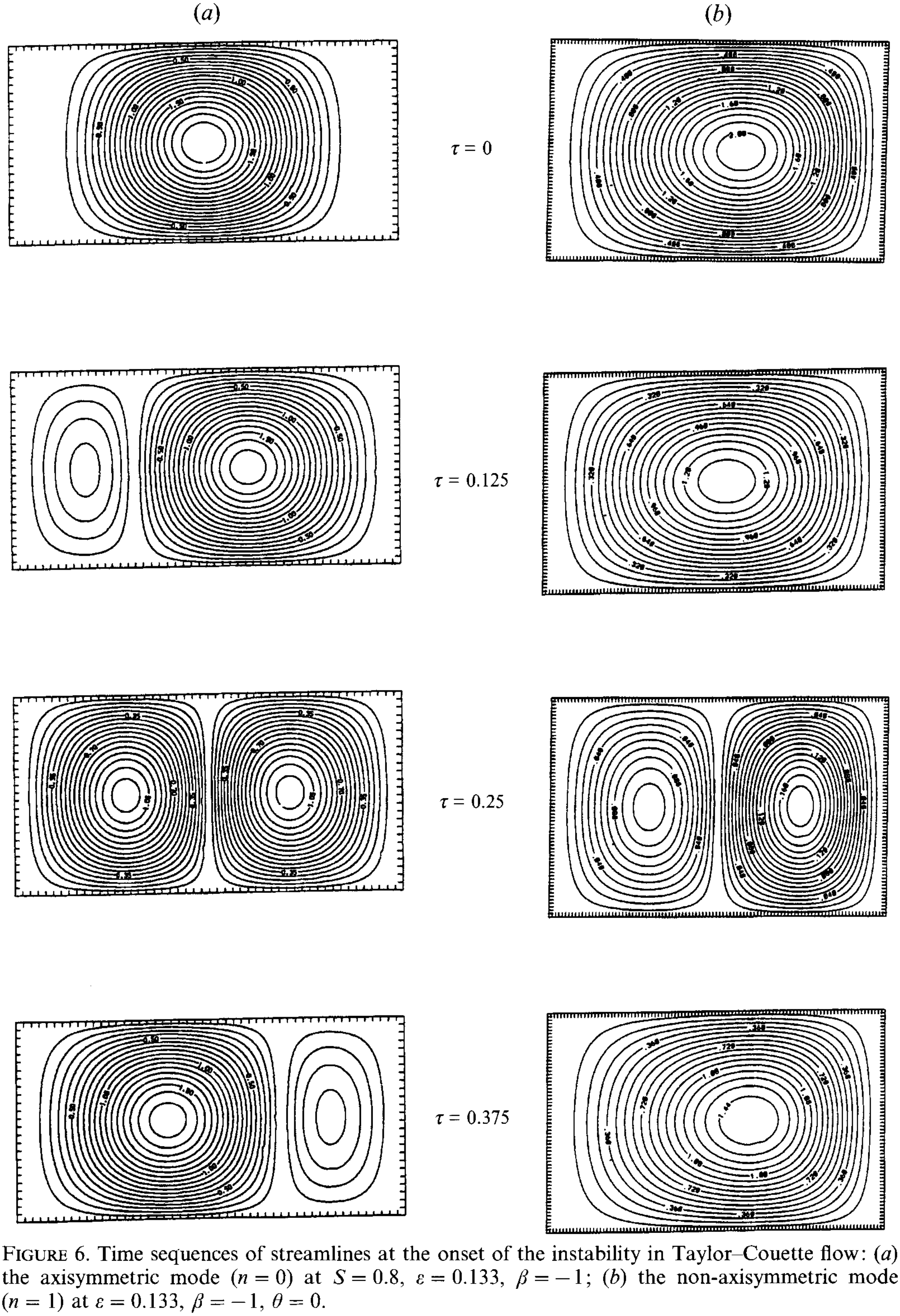

FIGURE 6. Time sequences of streamlines at the onset of the instability in Taylor–Couette flow: (*a*) the axisymmetric mode ($n = 0$) at $S = 0.8$, $\varepsilon = 0.133$, $\beta = -1$; (*b*) the non-axisymmetric mode ($n = 1$) at $\varepsilon = 0.133$, $\beta = -1$, $\theta = 0$.

the axisymmetric modes in Taylor–Dean flow can be found in our previous publication (Joo & Shaqfeh 1992).

2.4. *Energy analysis*: *mechanism of instability*

2.4.1. *Energy analysis*

Since our stability analysis predicts that certain non-axisymmetric modes are more unstable than the axisymmetric mode when the shearing by the cylinder rotation is the dominant flow driving force, we now investigate the mechanism of instability in purely elastic Taylor–Dean flow with respect to non-axisymmetric disturbances through an examination of the disturbance-energy equation. This energy method considers energy transfer between the mean flow and the disturbance flow by evaluating the mechanical energy balance for the system. We apply the same methodology as discussed in our previous publication (Joo & Shaqfeh 1992) where a detailed development of the energy equation can be found. The final dimensionless energy equation can be written (Joo & Shaqfeh 1992):

$$Re\left[(De)^{-1}\frac{\mathrm{d}E_k}{\mathrm{d}t}+\phi_{rey}\right]=\phi_{vis}-\frac{\mathrm{d}\varepsilon_p}{\mathrm{d}t}+De\phi_p. \tag{23}$$

In (23),

$$E_k=\frac{1}{2}\int \boldsymbol{v}'\cdot\boldsymbol{v}'\,\mathrm{d}\bar{V} \tag{24}$$

is the kinetic energy (per unit mass) of the disturbance,

$$\phi_{rey}=\int(\boldsymbol{v}'\cdot\nabla\boldsymbol{v}^0)\cdot\boldsymbol{v}'\,\mathrm{d}\bar{V} \tag{25}$$

is the rate of Reynolds stress energy production,

$$\phi_{vis}=\int(\nabla^2\boldsymbol{v}')\cdot\boldsymbol{v}'\,\mathrm{d}\bar{V} \tag{26}$$

is the total rate of viscous energy dissipation (both by polymer and solvent) which is always negative, and ε_p is the disturbance power created or dissipated by the action of the disturbance polymeric stresses:

$$\varepsilon_p=\int\boldsymbol{v}'\cdot\nabla\cdot\tau_p'\,\mathrm{d}\bar{V}. \tag{27}$$

Finally, ϕ_p represents the rate of energy production due to the elastic coupling between the perturbation flow and the base flow. This last term can be written

$$\phi_p=\phi_{pv1}+\phi_{pv2}+\phi_{ps}, \tag{28}$$

where

$$\phi_{pv1}=-\int\nabla\cdot(\boldsymbol{v}'\cdot\nabla\tau_p^0)\cdot\boldsymbol{v}'\,\mathrm{d}\bar{V} \tag{29}$$

is the rate of energy production caused by the coupling of the perturbation velocity and the base state polymeric stress gradient. Similarly, ϕ_{pv2} is the rate of energy production or dissipation caused by the coupling between the perturbation velocity gradient and the base state polymeric stresses:

$$\phi_{pv2}=\int\nabla\cdot[(\nabla\boldsymbol{v}')^T\cdot\tau_p^0+\tau_p^0\cdot\nabla\boldsymbol{v}']\cdot\boldsymbol{v}'\,\mathrm{d}\bar{V}. \tag{30}$$

The last term in (28)

$$\phi_{ps} = \int \nabla \cdot [(\nabla v^0)^T \cdot \tau'_p + \tau'_p \cdot \nabla v^0] \cdot v' \, \mathrm{d}\bar{V} \tag{31}$$

is the rate of the energy production caused by the coupling of the disturbance polymeric stresses to the base state velocity gradient.

In the limit as $Re \rightarrow 0$, (23) is not useful for determining the rate of change of the kinetic energy disturbance, $\mathrm{d}E_k/\mathrm{d}t$, because the kinetic energy and the energy production term due to Reynolds stresses ϕ_{rey} are always vanishingly small relative to the energy production or dissipation created by the viscous or elastic stresses (i.e. the right-hand side of (23)). In this limit, if we consider the total rate of work done by the disturbance flow,

$$\int v' \cdot \nabla \tau' \, \mathrm{d}\bar{V} = S \int (\nabla^2 v') \cdot v' \, \mathrm{d}\bar{V} + De \int v' \cdot \nabla \tau'_p \, \mathrm{d}\bar{V} = 0, \tag{32}$$

we obtain the following relation:

$$\frac{\mathrm{d}\varepsilon_p}{\mathrm{d}t} = S \frac{\mathrm{d}}{\mathrm{d}t} \int \nabla v' : \nabla v' \, \mathrm{d}\bar{V}. \tag{33}$$

Thus, $\mathrm{d}\varepsilon_p/\mathrm{d}t$ is the rate of change of the absolute value of the power dissipated by the solvent. Since one expects on physical grounds that as the perturbation velocity grows, more energy will be dissipated by the solvent, we expect the sign of $\mathrm{d}\varepsilon_p/\mathrm{d}t$ to indicate growth or decay in the magnitudes of the perturbation fields, and hence, instability or stability. To be more specific, the rate of change of the positive definite norm $\int \nabla v' : \nabla v' \, \mathrm{d}\bar{V}$ plays a role in the energy analysis of these stress-driven instabilities analogous to that $\int v' \cdot v' \, \mathrm{d}\bar{V}$ plays in the analysis of inertial instabilities. Note that by independently calculating $\int v' \cdot v' \, \mathrm{d}\bar{V}$ our results show that $(\mathrm{d}/\mathrm{d}t) \int \nabla v' : \nabla v' \, \mathrm{d}\bar{V}$ is always of the same sign as $(\mathrm{d}/\mathrm{d}t) \int v' \cdot v' \, \mathrm{d}\bar{V}$ for these elastic instabilities (Joo & Shaqfeh 1992). We thus have the following energy equation in the limit as $Re \rightarrow 0$:

$$\frac{\mathrm{d}\varepsilon_p}{\mathrm{d}t} = \phi_{vis} + De \, \phi_p. \tag{34}$$

We have reported that when the disturbance flow is axisymmetric, the mechanism for the elastic, stationary instability in Taylor–Dean flow is associated with the coupling of the perturbation velocity field to the polymeric normal stress gradients in the base flow (ϕ_{pv1} in the energy equation (34)), while the mechanism for the elastic, oscillatory instability in Taylor–Dean flow involves the coupling between the disturbance polymeric stresses and the base state velocity gradients (ϕ_{ps} in the energy equation (34)) (Joo & Shaqfeh 1992). Although the final energy equation (34) remains the same for the non-axisymmetric disturbances, the three energy production terms ϕ_{pv1}, ϕ_{pv2}, and ϕ_{ps} include additional terms which arise from the azimuthal variations of the disturbance flow. Thus, we are interested in how these new additional terms will make contributions to energy production or dissipation especially when the non-axisymmetric modes are more unstable than the axisymmetric mode. In the following discussion we concentrate exclusively on the energy balance for the two-dimensional circulation flow in the (x, z)-plane. As discussed elsewhere (Joo & Shaqfeh 1992), we have identified this balance as the key to understanding the mechanism of instability in these flows.

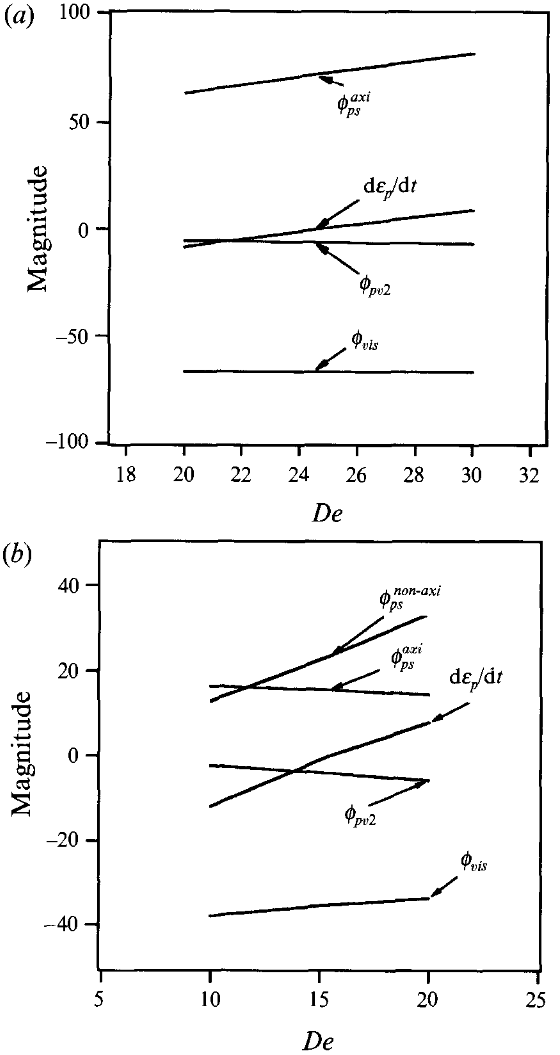

FIGURE 7. The terms in the energy equation (34) in Taylor–Couette flow (*a*) with respect to axisymmetric disturbances, and (*b*) with respect to non-axisymmetric disturbances.

In figure 7 we have plotted the terms in the energy equation (34) over a given range of *De* (both sub- and supercritical values) for elastic Taylor–Couette flow both when the disturbance flow is axisymmetric (figure 7*a*) and when it is non-axisymmetric (figure 7*b*). The energy production due to the coupling between the disturbance polymeric stresses and the base state velocity gradients ϕ_{ps}^{axi} is shown to be the mechanism in Taylor–Couette flow, if the disturbance flow is axisymmetric (Joo & Shaqfeh 1992). When the disturbance flow is non-axisymmetric, however, the same term ϕ_{ps}^{axi} decreases, while a new contribution to the energy production caused by the azimuthal variation of the disturbance flow $\phi_{ps}^{non\text{-}axi}$ increases considerably as *De* passes the critical value 15.2 (see figure 7*b*). Thus, this new contribution $\phi_{ps}^{non\text{-}axi}$ appears to control the onset of instability in Taylor–Couette flow if the disturbance flow is non-axisymmetric. This indicates a new instability mechanism since $\phi_{ps}^{non\text{-}axi}$ is entirely absent when the disturbance flow is axisymmetric. Although there is a small additional coupling between the perturbation velocity gradient and the base state polymer stresses

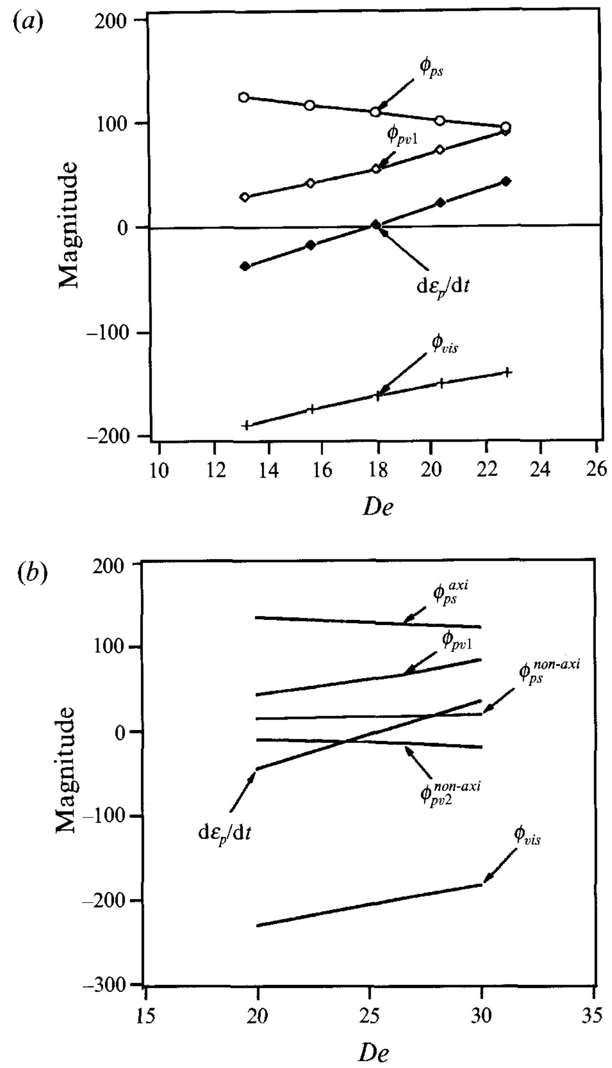

FIGURE 8. The terms in the energy equation (34) in Dean flow (*a*) with respect to axisymmetric disturbances, and (*b*) with respect to non-axisymmetric disturbances.

($\phi_{pv2}^{non\text{-}axi}$) owing to the azimuthal variation of the disturbance flow, we find that the term ϕ_{pv2} results only in a small energy dissipation for both axisymmetric and non-axisymmetric disturbances.

In figure 8, we have plotted the terms in (34) over a given range of *De* for elastic Dean flow both when the disturbance flow is axisymmetric (figure 8*a*) and when it is non-axisymmetric (figure 8*b*). When the disturbance flow is axisymmetric, the coupling of the perturbation velocity field to the polymeric normal stress gradients in the base flow ϕ_{pv1} appears to control the onset of the instability, and there is no energy dissipation or production due to the coupling between the perturbation velocity gradient and the base state polymer stresses ($\phi_{pv2} = 0$). When the disturbance flow is non-axisymmetric, the same term ϕ_{pv1} increases with increasing *De* through the critical value. We find that the azimuthal variation of the disturbance flow does not contribute to the coupling of the perturbation velocity field and the polymeric normal stress gradients in the base

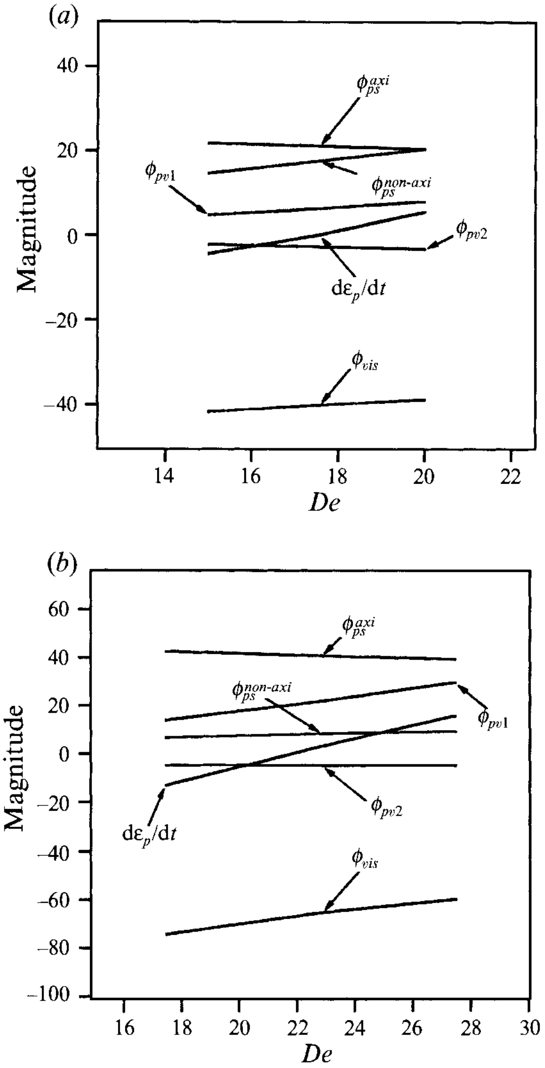

FIGURE 9. The terms in the energy equation (34) in Taylor–Dean flow (*a*) with respect to non-axisymmetric disturbances, and (*a*) when the shearing by cylinder rotation is the dominant flow-driving force ($\delta = 0.25$), and (*b*) when the azimuthal pressure gradient is dominant ($\delta = 0.75$).

flow ϕ_{pv1}. The additional terms due to the azimuthal variation of the disturbance flow $\phi_{ps}^{non\text{-}axi}$ and $\phi_{pv2}^{non\text{-}axi}$ result only in small energy production and dissipation, respectively.

Finally, we have plotted the terms in the energy equation (34) for Taylor–Dean flows in figure 9, when the disturbance flow is non-axisymmetric. When the shearing by the cylinder rotation is the dominant flow-driving force ($\delta = 0.25$ in figure 9*a*), the terms in figure 9(*a*) are similar to those calculated for Taylor–Couette flow: the contribution to the energy production $\phi_{ps}^{non\text{-}axi}$ tracks with the rate of change of the power created by the disturbance polymeric stresses $d\varepsilon_p/dt$. The coupling of the perturbation velocity field to the polymeric normal stress gradients in the base flow ϕ_{pv1} exists but is small compared to $\phi_{ps}^{non\text{-}axi}$. When the pressure gradient is the dominant flow driving force ($\delta = 0.75$ in figure 9*b*), the terms in figure 9(*b*) are similar to those calculated for Dean flow: the energy production term ϕ_{pv1} becomes dominant and tracks with $d\varepsilon_p/dt$. The

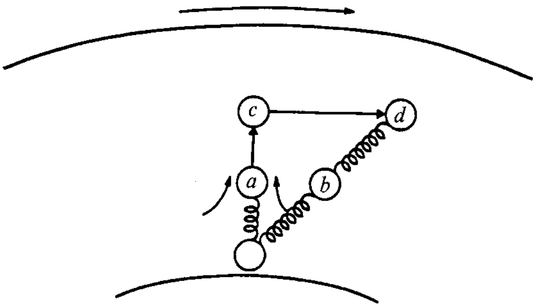

FIGURE 10. Mechanism of instability in Taylor–Couette flow with respect to axisymmetric disturbances: with no secondary flow, the base flow deflects a bead of an elastic dumb-bell from *a* to *b*. With a secondary radial flow, the dumb-bell is stretched in the radial direction, and the base flow then deflects the bead farther; i.e. from *c* to *d* (Larson *et al.* 1990).

term $\phi_{ps}^{non\text{-}axi}$ becomes small, but increases as De passes the critical value 22.9, and the term ϕ_{pv2} again results in small energy dissipation.

In conclusion, the additional coupling between the disturbance polymeric stresses and the base state velocity gradients due to the azimuthal variation of the disturbance flow controls the onset of Taylor–Dean flow instability with respect to non-axisymmetric disturbances, when the shearing by the cylinder rotation is the dominant flow driving force. As the azimuthal pressure gradient becomes dominant, this coupling becomes insignificant and the coupling of the perturbation velocity field to the polymeric normal stress gradients in the base flow controls the onset of instability. In the next subsection, we analyse the mechanism of instability to non-axisymmetric modes in Taylor–Dean flows and show that it arises from the interplay between the disturbance polymeric stresses due to the azimuthal variation of the disturbance flow and the base state velocity gradients.

2.4.2. *New mechanism of viscoelastic instability*

Based on the results of the energy analysis described above, a new mechanism for the viscoelastic Taylor–Couette flow instability with respect to non-axisymmetric disturbances has been discovered. It is associated with the coupling between the disturbance polymeric stress due to the azimuthal variation of the disturbance flow and the base state velocity gradient. To be more specific, the coupling between the gradient of the azimuthal velocity in the base state ($\partial v_\theta^0/\partial r$) and the perturbation shear stress ($R\theta$) creates an elastic 'hoop' stress $\theta\theta$, and this controls the onset of instability. It should be noted that the mechanism associated with axisymmetric disturbances in Taylor–Couette flow is also dependent on this coupling. However, when the disturbance flow is non-axisymmetric, the development of the perturbation shear stress $R\theta$ in this coupling is very different from that associated with axisymmetric disturbances. In order to demonstrate the differences in the mechanism of instability in these two cases, we first recapitulate the mechanism associated with axisymmetric disturbances and then analyse the new mechanism of the Taylor–Couette flow instability with respect to non-axisymmetric disturbances.

The mechanism of the instability can most easily be understood by referring to the dumb-bell model from which the Oldroyd-B constitutive equation is derived as described by Larson *et al.* (1990). For the axisymmetric disturbances, the radial extensional flow ($\partial U/\partial r$) stretches the dumb-bell in the r-direction (see figure 10). Owing to the base shearing flow, this additional stretching of the dumb-bell in the r-direction (e.g. increase in radial normal perturbation stress RR) causes the development

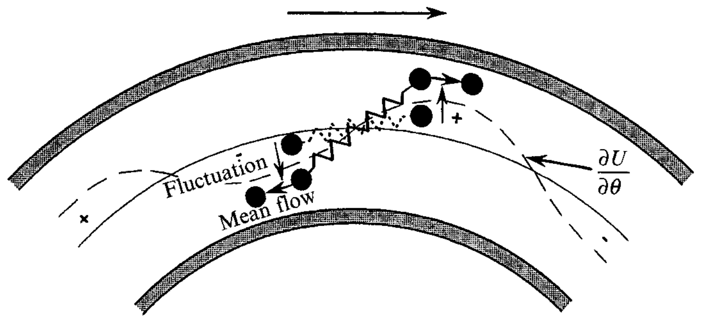

FIGURE 11. Mechanism of instability in Taylor–Couette flow with respect to non-axisymmetric disturbances: owing to its azimuthal variation, the radial perturbation velocity U deflects the beads of an elastic dumb-bell in the radial direction, which causes the development of perturbation shear stress $R\theta$. The development of perturbation shear stress couples to the base shearing flow to deflect the beads farther leading to an increased stretch of the dumb-bell in the azimuthal direction.

of the perturbation shear stress $R\theta$. This development of the perturbation shear stress $R\theta$ couples to the base shearing flow to produce an increased stretch of the dumb-bell in the azimuthal direction (i.e. increase in the hoop stress $\theta\theta$). Because the streamlines are curvilinear, this elastic 'hoop' stress reinforces the radial perturbation flow leading ultimately to a secondary toroidal vortex flow (see figure 10) (Larson *et al.* 1990).

When the disturbance flow is non-axisymmetric, the development of the perturbation shear stress $R\theta$ in the term ϕ_{ps} occurs through a different pathway. First, the coupling between the radial perturbation velocity gradient in the azimuthal direction $(\partial U/\partial \theta)$ and the azimuthal normal stress in the base state $(\tau^0_{\theta\theta})$ causes the development of the $R\theta$ shear stress: the radial perturbation velocity U which varies along the azimuthal direction deflects the beads of an elastic dumb-bell in the radial direction (see figure 11). This deflection causes the perturbation shear stress $R\theta$ to develop, and this development of the perturbation shear stress then couples to the base shearing flow to produce an increased stretch of the dumb-bell in the azimuthal direction (e.g. increase in the hoop stress $\theta\theta$) (see figure 11). It should be noted that the coupling of the azimuthal variation of the radial perturbation velocity to the azimuthal normal stress in the base state is crucial in the mechanism described above.

As a constant azimuthal pressure gradient is added to Taylor–Couette flow to produce a Taylor–Dean flow, the average base state values of the azimuthal velocity gradient, $\partial v^0_\theta/\partial r$, and stress (shear $(\tau^0_{r\theta})$ and azimuthal normal $(\tau^0_{\theta\theta})$) made dimensionless with the product of the gap and the maximum shear rate across the gap decrease monotonically (Joo & Shaqfeh 1992). Therefore, the coupling described above and present in the term $\phi^{non\text{-}axi}_{ps}$ decreases as the pressure gradient is increased. Finally, the mechanism described in figure 11 is suppressed by the coupling between the perturbation velocity field and the polymeric normal stress gradients in the base flow ϕ_{pv1}, as the pressure gradient becomes the dominant flow driving force.

3. The effects of the gap width

If we relax the small-gap assumption, the linear stability equations governing small non-axisymmetric disturbances in the Taylor–Dean flow of an Oldroyd-B fluid are rather lengthy and cumbersome. These equations are given in the Appendix. For brevity, we shall only discuss the stability results with finite-gap width in elastic Taylor–Couette and Dean flows. The effects of finite gap are very similar in Taylor–Dean flows and are discussed elsewhere (see Joo 1993). First, the calculations

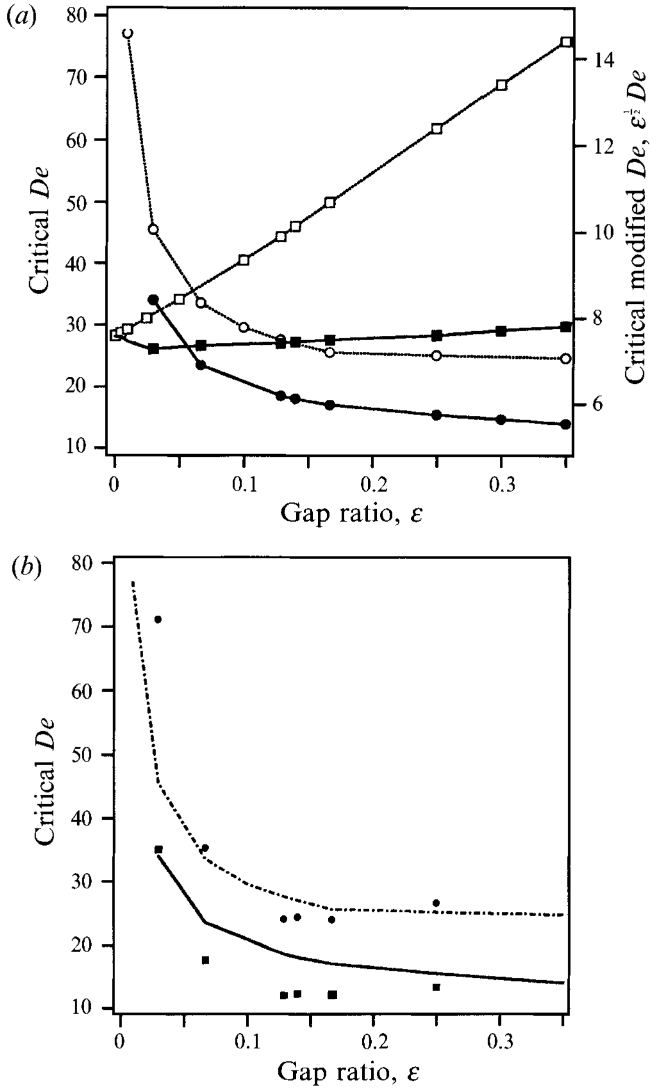

FIGURE 12. The critical Deborah numbers *vs.* the gap ratio as predicted by the linear stability theory for Taylor–Couette flow at $S = 0.79$. (*a*) Theoretical predictions for both axisymmetric and non-axisymmetric modes are shown for the theory including finite-gap effects. · · · ○ · · ·, finite gap (axisymmetric); ——●——, finite gap. *De* (non-axisymmetric); · · · □ · · ·, Mod. *De* (axisymmetric); ——■—— Mod. *De* (non-axisymmetric). (*b*) The data from Larson *et al.* (1990) are included. Note that two different experimental values of De_{cr} based on two different polymer relaxation times are shown: the relaxation time determined from steady-state normal stresses was used for the lower value of De_{cr}, and the relaxation time from relaxation of normal stresses after cessation of steady shear was used for the higher value of De_{cr}. · ·——·——· ·, finite gap (axisymmetric); ●, data 1 (PIB/PB Boger fluid); ■, data 2 (PIB/PB Boger fluid); ——, finite gap (non-axisymmetric).

for Taylor–Couette flow are presented for gap ratios in the range $0 < \varepsilon \leqslant 0.35$ (figure 12*a*). These are then compared with the experimental results by Larson *et al.* (1990) (figure 12*b*). We choose the value of $S = \eta_s/\eta_t = 0.79$ which corresponds to the PIB/PB boger fluid used in their experiments. In addition, again following the experiments of Larson *et al.* (1990), β was set to -1 which corresponds to the case when only the inner cylinder rotation drives the flow. A summary of the critical

Concentration (p.p.m.)	$S = \eta_s/(\eta_s+\eta_p)$	Critical shear rate (s^{-1})	Critical *De* from λ_s	Critical *De* from λ_t	Critical *De* from theory
0	—	> 46	—	—	—
1000	0.8630	7.4	9.4	28	24.1
2000	0.7368	2.8	8.9	27	18.9
4000	0.6154	1.4	7.0	17	17.0
6000	0.5000	0.9	7.2	17	16.3

TABLE 2. Concentration dependence of the critical conditions for Taylor–Couette flow ($\beta = -1$, $\epsilon = 0.1$, PS/PS/DOP Boger fluid). The critical Deborah numbers for the non-axisymmetric mode at four different values of S are compared with the experimental data by Shaqfeh *et al.* (1992). λ_s and λ_t represent the polymer relaxation time from steady-state normal stresses and from relaxation of normal stresses after cessation of steady shear, respectively.

Deborah numbers for both axisymmetric ($n = 0$) and non-axisymmetric ($n = 1$) modes of the elastically-driven instability in Taylor–Couette flow is found in figure 12. For both axisymmetric and non-axisymmetric modes, the calculations with finite-gap width are shown in figure 12*a*. Beyond the small-gap limit, the shear rate ceases to be constant across the gap, and thus it is natural to define the Deborah number in the finite-gap calculations as the product of the fluid relaxation time λ and the shear rate at the inner cylinder as has been done by Shaqfeh *et al.* (1992), namely

$$De = \dot{\gamma}\lambda = \frac{2|\beta|(1+\epsilon)^2}{(1+\epsilon)^2-1}\Omega_1\lambda. \tag{35}$$

The right-hand side of (35) is equal to the product of the constant shear rate across the gap and the polymer relaxation time in the limit of small gap. In figure 12(*a*) we have referred to the product $\epsilon^{\frac{1}{2}}De$ as the modified Deborah number and we further note that this parameter plays the analogous role of the Taylor number in the centrifugally driven Newtonian instability (see Chandrasekar 1961; Drazin & Reid 1981). Figure 12(*a*) demonstrates that, in terms of $\epsilon^{\frac{1}{2}}De$, finite-gap effects are monotonically stabilizing, generally increasing the critical value of $\epsilon^{\frac{1}{2}}De$ for both axisymmetric and non-axisymmetric modes. However, the rate of increase in $\epsilon^{\frac{1}{2}}De$ with increasing gap is slower in the case of the non-axisymmetric mode. It should also be noted that the critical wavenumber increases as the gap ratio ϵ is increased.

In figure 12(*b*) we present the experimental data of Larson *et al.* (1990). Note that a polyisobutylene/polybutene/trichloroethylene Boger fluid was used in their experiments which is similar to that used in our experiments presented in §5. The two experimental values of De_{cr} in figure 12(*b*) correspond to the values based on two different polymer relaxation times: the relaxation time determined from steady-state normal stresses was used for the lower value of De_{cr}, and the relaxation time from relaxation of normal stresses after cessation of steady shear was used for the higher value of De_{cr}. This difference in the polymer relaxation time has been discussed elsewhere (e.g. Magda & Larson 1988; Larson *et al.* 1990), and will be discussed in §4 for our experimental fluids. It is observed that the theoretical predictions for the non-axisymmetric mode lie between these two experimental data.

Meanwhile, the polymer concentration dependence of the critical conditions is shown in table 2, where the critical Deborah numbers for the non-axisymmetric mode at four different values of S are compared with the experimental data using a PS/PS/DOP Boger fluid by Shaqfeh *et al.* (1992). It is found that the theoretical

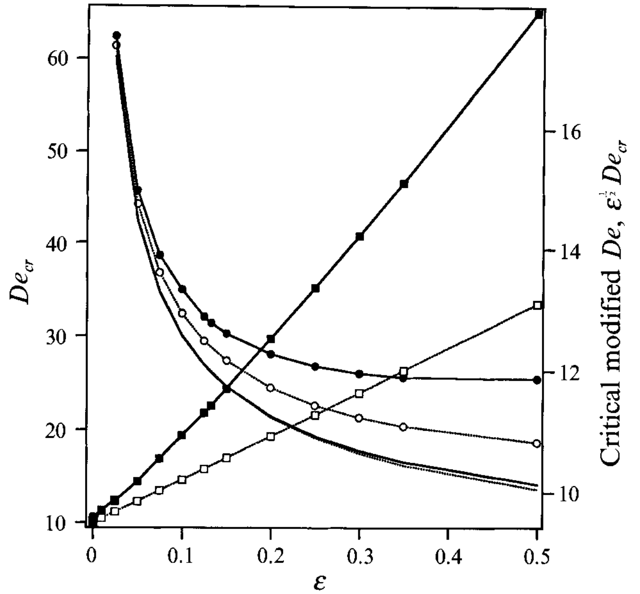

FIGURE 13. The critical Deborah number *vs.* the gap ratio as predicted by the linear stability analysis calculations for Dean flow at $S = 0.79$. Theoretical predictions for both axisymmetric and non-axisymmetric modes are shown in the limit of small gap and for the theory including finite-gap effects. ···○···, finite gap (axisymmetric); ......, narrow gap (axisymmetric); ——●——, finite gap (non-axisymmetric); ——, narrow gap (non-axisymmetric); ···□···, Mod De (axisymmetric); ——■——, Mod De (non-axisymmetric).

predictions are in good agreement with the experimental data when we base our comparison on the relaxation time measured from the relaxation of normal stresses after cessation of steady shear.

In figure 13, the calculations for Dean flow are presented for the gap ratios in the range $0 < \varepsilon \leqslant 0.5$. The critical Deborah numbers for both axisymmetric ($n = 0$) and non-axisymmetric ($n = 1$) modes are shown, and the calculations with the finite-gap width are compared with those in the narrow-gap limit for both axisymmetric and non-axisymmetric modes. At a fixed gap ratio ε ($\varepsilon > 10^{-4}$), the critical Deborah number of the axisymmetric mode is slightly lower than that of the non-axisymmetric mode in the narrow-gap limit. However, the calculations for a finite gap show that the critical De_{cr} of the axisymmetric mode is in fact much lower than that of the non-axisymmetric mode at a fixed gap ratio. Thus, the axisymmetric mode is always significantly more unstable than the non-axisymmetric mode at a fixed geometry. Figure 13 also demonstrates that, in terms of $\varepsilon^{\frac{1}{2}}De$, finite-gap effects are monotonically stabilizing, generally increasing the critical value of $\varepsilon^{\frac{1}{2}}De$ for both axisymmetric and non-axisymmetric modes. However, the rate of increase in $\varepsilon^{\frac{1}{2}}De$ with increasing gap is slower in the case of the axisymmetric mode. Note that as the gap becomes smaller ($\varepsilon \rightarrow 0$), the critical conditions $\varepsilon^{\frac{1}{2}}De$ approach each other for axisymmetric and non-axisymmetric modes. As we have previously discussed, this is due to the fact that the terms which differentiate the stability characteristics of the two different mode types are $O(\varepsilon^2 De^3)$ and these approach zero like $\varepsilon^{\frac{1}{2}}$ as $\varepsilon \rightarrow 0$, if $\varepsilon^{\frac{1}{2}}De \sim O(1)$. It should also be noted that the critical wavenumber decreases as the gap ratio ε is increased.

4. Experimental procedures

4.1. *Fluid preparation and characterization*

The highly elastic fluid used in the following experiments was a polybutylene/polybutene 'Boger fluid'; i.e. a small amount of a high molecular weight polymer dissolved in a viscous, Newtonian solvent. The high-molecular-weight species was a polyisobutylene with a weight average molecular weight of 4 to 6 million and a broad molecular weight distribution (Magda & Larson 1988; Larson *et al.* 1990). It was dissolved in trichloroethylene and this solution was added to a low molecular weight polybutene. The trichloroethylene was evaporated in a vacuum oven for four weeks. The final concentration of polyisobutylene in the solution was 1000 p.p.m. A very similar PIB/PB Boger fluid has been used in other viscoelastic flow experiments (e.g. Larson *et al.* 1990; McKinley, Byars & Brown 1991*a*).

The rheology of this Boger fluid was thoroughly characterized on the Rheometrics Dynamic Analyzer II rheometer. Throughout these experiments the temperature was maintained at 20.0 ± 0.5 °C via a convection oven. The steady shear viscosity and primary normal stress coefficient measurements are presented in figure 14. These steady shear material functions show nearly Oldroyd-B behaviour in the range of shear rate: $1 \leqslant \dot{\gamma} \leqslant 10\ \mathrm{s}^{-1}$. We note that the shear rates in the Taylor–Dean experiments in §5 are well within this range (see figure 23*a* and figure 24*a*). The total shear viscosity is about 250 poise and Ψ_1 is 600 dyne $\mathrm{s}^2/\mathrm{cm}^2$ in this shear rate range. The dynamic viscosity η' in small-amplitude oscillatory shearing is shown as a function of frequency in figure 15. For the Oldroyd-B model, we have

$$\eta' = \frac{\eta_p}{1+\lambda^2\omega^2} + \eta_s, \quad \Psi_1 = 2\lambda\eta_p, \tag{36}$$

and thus interpreting the data in terms of this model $\eta_s = 200$ poise, $\eta_p = 50$ poise, and $\lambda = 6$ s, respectively. The dynamic viscosity for an Oldroyd-B fluid given by the above expression is also plotted in figure 15. The experimental values for η' decrease more gradually with ω than predicted: this is indicative of a broad spectrum of relaxation times in the polydisperse fluid, as discussed elsewhere (Larson *et al.* 1990; Quinzani *et al.* 1991). Since alternate measurements weight the various relaxation times in the spectrum differently, a different average value of the relaxation time can be obtained by fitting the Oldroyd-B model to other experimental measurements. A fit of the Oldroyd-B model to the relaxation of the normal force in a plate-and-plate or cone-and-plate measuring device gives a value of $\lambda \approx 13$ s, which is about twice the value found from the steady-state normal stress measurement (see figure 16). This difference in the average relaxation time has been observed in other studies (e.g. Magda & Larson 1988; Larson *et al.* 1990). Magda & Larson (1988) found in their study of elastic instabilities in cone-and-plate and plate-and-plate flows that the value De_{cr} based on the relaxation time measured in transient experiments was in much better agreement with the theoretical predictions than a similar comparison based on a relaxation time calculated from steady-state normal forces or normal stress differences. Larson *et al.* (1990) have also made similar observations in their study of elastic Taylor–Couette instabilities. Thus, we shall choose an average relaxation time based on the decay of the primary normal stress difference after cessation of steady shear to compare our theory with experiment.

4.2. *Taylor–Dean apparatus*

An apparatus was constructed to generate a spectrum of Taylor–Dean flows by placing a stationary, meridional obstruction between independently rotating, concentric

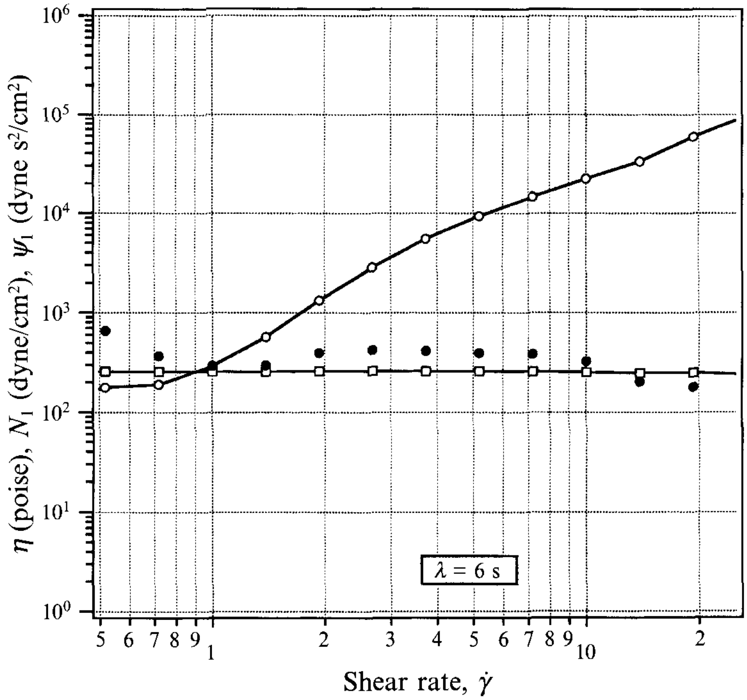

FIGURE 14. The steady shear viscosity η, the first normal stress N_1 and the first normal stress coefficient Ψ_1 as a function of the shear rate $\dot{\gamma}$ for the 1000 p.p.m. PIB/PB Boger fluid used in our experiments. ——□——, η; ——○—— N_1; ●, Ψ_1.

cylinders. The inner cylinder radius, R_1 was 7.5 cm and the height of the inner cylinder was 20 cm. The outer cylinder has an inner radius of 8.5 cm, so that the dimensionless gap $\varepsilon = (R_2 - R_1)/R_1$ was equal to 0.133. While the cylinders are assumed to be infinitely long in the stability analysis in §2, the height to gap ratio of the apparatus is 20. We note that this number is larger than the ratio of the inner cylinder radius to the gap, 7.5, and the finite-length effects have not been considered in this current study. The top of the cell is stationary, while the bottom moves with the outer cylinder, and the variation in the gap with the axial position was negligible. The block generates an azimuthal pressure gradient in opposition to the shearing flow as shown in figure 17(a). From the condition of material conservation across a given radial section in the apparatus, the azimuthal pressure gradient can be related to the rotation rates of inner and outer cylinders via the expression (see Joo 1993):

$$\xi = -\frac{\partial P}{\partial \theta} \frac{d^2}{2\eta_t R_1^2 \Omega_1} = \frac{3\Omega_1 + 3\Omega_2}{\Omega_1}. \tag{37}$$

Thus, for $\beta > 0$, we have the following expression for δ in terms of the rotation rates of inner and outer cylinders:

$$\delta = \frac{\xi}{\xi + \beta} = \frac{3\Omega_1 + 3\Omega_2}{2\Omega_1 + 4\Omega_2}. \tag{38}$$

For $\beta < 0$, we have a similar expression for δ^*:

$$\delta^* = \frac{\xi}{\xi - \beta} = \frac{3\Omega_1 + 3\Omega_2}{4\Omega_1 + 2\Omega_2}. \tag{39}$$

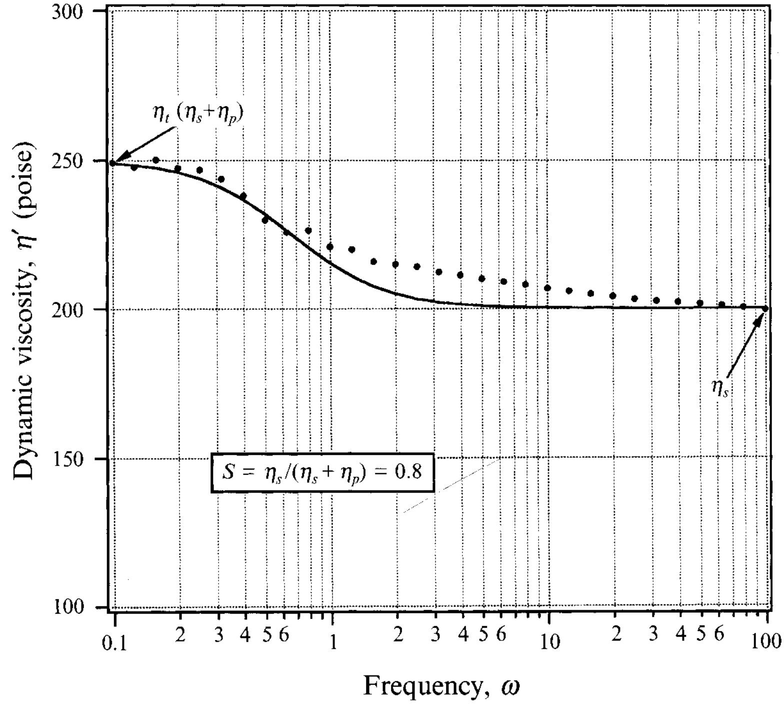

FIGURE 15. The dynamic viscosity η' as a function of frequency ω in small-amplitude oscillatory shearing for the 1000 p.p.m. PIB/PB Boger fluid (symbols). The line is the prediction of the Oldroyd-B model. ●, experimental data; ——, Oldroyd fluid.

Therefore, counter-rotating the cylinders ($\Omega_2 = -\Omega_1$) generates Taylor–Couette flow ($\delta = \delta^* = 0$, figure 17*b*), while co-rotating the cylinders ($\Omega_2 = \Omega_1$) generates Dean flow ($\delta = \delta^* = 1$, figure 17*c*). In addition, by changing the ratio of the rotation rate of the inner cylinder to the outer cylinder, a complete series of Taylor–Dean flows can be obtained. It should be noted that in the Dean flow generated in our apparatus, the maximum velocity occurs at the cylinders, while in the classical Dean flow it occurs at the centre of the gap (cf. figure 17*c* and figure 1*b*). However, we shall not distinguish between these two flows, since the velocity gradient which plays a major role in elastic instabilities in curved streamlines is identical for both cases. It is found that the critical Deborah number and the critical wavenumber are the same no matter where the maximum velocity lies (or more specifically if we add an arbitrary constant azimuthal flow), while the frequency of oscillation for the non-axisymmetric modes varies slightly (see Joo 1993).

4.3. *Flow visualization and image analysis*

Flow visualization experiments and laser-Doppler velocimetry (LDV) measurements were performed in this flow cell in order to study the onset of flow instability. In our flow visualization experiments, mica flakes about 60 μm in length were suspended in the fluid; these plate-like particles reflect light in a manner that is highly dependent on their orientation so that their alignment by the flow results in variations in the reflected light intensity. The flow dynamics were recorded on videotape by using a high resolution video-camera. This video signal is sent to a Macintosh computer in which the image is digitized by a frame grabber card (QuickImage, Mass Microsystems) at a rate of 1 frame per $\frac{1}{30}$ s. In addition, an axial intensity profile can be obtained by

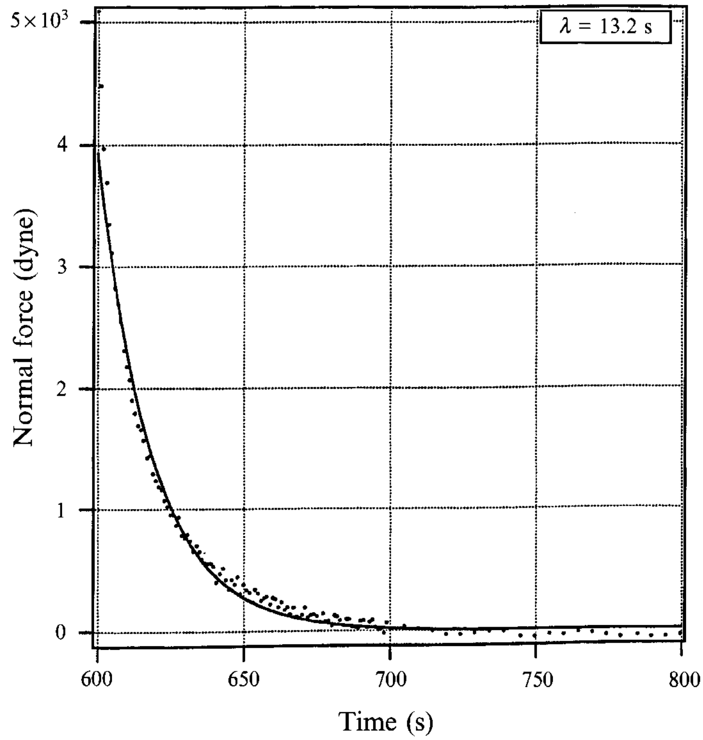

FIGURE 16. Relaxation of normal force after cessation of steady state shearing for the Boger fluid. The line is a fit for the Oldroyd-B equation, i.e. a single exponential decay. ●, transient data; ——, single exponential fitting.

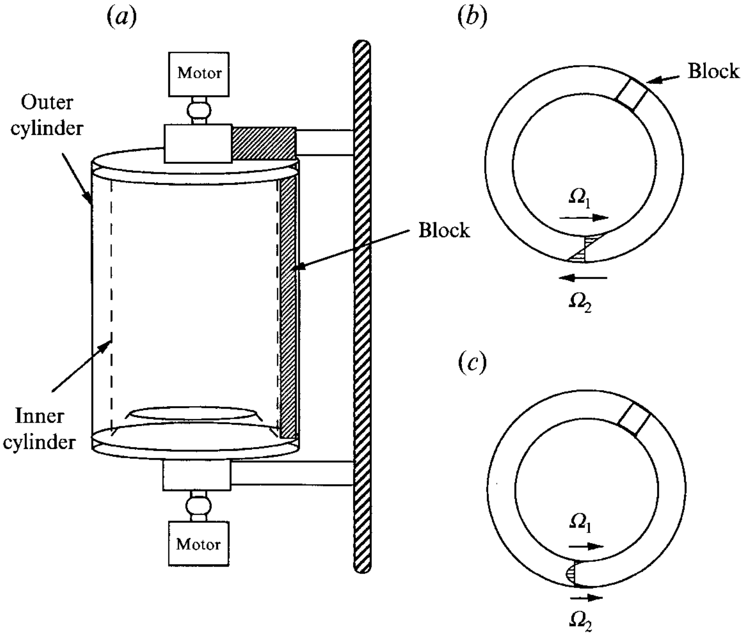

FIGURE 17. Taylor–Dean apparatus in which a stationary, meridional obstruction is placed between independently rotating, concentric cylinders to generate an azimuthal pressure gradient in opposition to the shearing flow. (*a*) Flow cell. (*b*) Taylor–Couette flow (counter-rotation). (*c*) Dean flow (co-rotation).

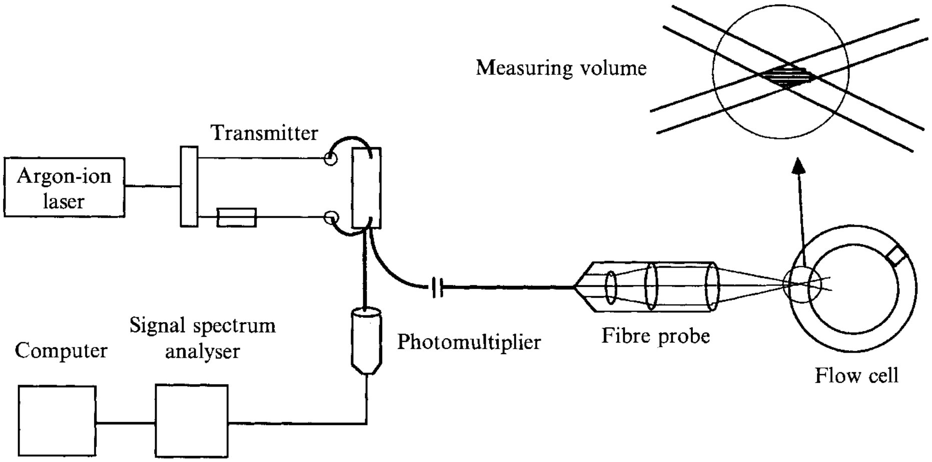

FIGURE 18. Laser-Doppler velocimetry (LDV) system.

examining one pixel column of the digitized image. The wavenumber is then determined by taking a fast Fourier transform of the intensity profile. Thus, unlike previous flow-visualization experiments on elastic instabilities in which only qualitative information was obtained (e.g. Larson *et al.* 1990; McKinley *et al.* 1991*b*), this spectral image analysis provides a direct measure of the wavenumber.

4.4. *Laser-Doppler velocimetry*

The basic components of the LDV system are indicated schematically in figure 18. We used a two-beam, one-component system. The 514.5 nm green line of a 300 mW, Argon-Ion laser (Dantec Fiberflow system) is split, and the frequency of one of the split beams is then shifted by 40 MHz. The beams are subsequently manipulated by a series of transmitting optics and optical fibres. These two beams are directed through a final focusing lens which causes the beams to intersect at the lens focal point to form a measuring volume or 'fringe pattern'. A particle moving with the fluid and passing through the measuring volume scatters light at a frequency that is Doppler-shifted relative to the incident light owing to the movement of the particle. The magnitude of the frequency shift is directly proportional to the tracer particle's velocity and hence provides a non-invasive measure of the local fluid velocity. The measuring volume dimensions were 36 μm × 36 μm × 228 μm, with the long axis of the ellipsoidal volume lying along the optical axis of the system. Since each measurement is an average over this volume, these dimensions allow us to measure up to 27 data points across the gap between the cylinders. The scattered light is collected in the photomultiplier through the same lens used for the transmitting optics. The signal from the photomultiplier is sent to a spectrum analyser (Dantec 57N10). Finally, the output of the analyser is manipulated in our lab computer. This LDV system was used to measure the base state azimuthal velocity in Taylor–Dean flow. The root-mean-square of the velocity measurements at each point was less than 0.075 mm/s. This value is less than 3% of the maximum velocity of the flow. It was also used to determine the frequency of the oscillation of the disturbance flow by measuring the axial velocity for a long period of time at super-critical flow conditions.

5. Experimental results

First, in §5.1, we present the base state azimuthal velocity in Taylor–Dean flow obtained from our LDV measurements. These results demonstrate that our apparatus does produce the base velocity field as predicted by the theory at least when measurements are taken away from the vicinity of the block itself. Then, detailed flow visualization results following the flow transition are presented in §5.2. The critical wavenumber obtained from spectral image analysis, and the critical Deborah number are compared with the theoretical predictions for various ratios of the pressure gradient to shear flow driving force. Finally, in §5.3, we show the time-dependent LDV measurements of axial velocities at super-critical conditions. This determines whether the vortex flow at the onset of the Taylor–Dean instability is oscillatory. The comparison between experiments and the linear stability theory in §§5.2 and 5.3 is made under the assumption that the transition to the nonlinear state is super-critical, so that the characteristics of the secondary flow are well described by the linear theory. Using the nonlinear analysis together with the LDV amplitude measurements, studies of the nonlinear effects on these elastic instabilities are currently underway to determine how nonlinearities influence characteristics of the secondary flow such as the saturation amplitudes and wavenumbers (Joo & Shaqfeh 1993).

5.1. *Base state velocity profiles*

The velocity field obtained by co-rotating the cylinders at the same velocity was measured at various azimuthal positions. The rotation speed of the inner and outer cylinders was slowly increased to a final velocity which was below that predicted to produce the viscoelastic instability. The results are shown in figure 19, where the azimuthal velocity is shown as a function of radial position. The results are in good agreement with the predictions of the Oldroyd-B model, shown as the solid curve in the figure. The error bars in figure 19 indicate the errors in the mean determined from a time series measurement taken at various points along the gap. The base flow is shown to be a purely azimuthal, steady, parabolic Dean flow except near the block. By changing the ratio of the rotation rate of the inner cylinder to the outer cylinder, the base state velocity fields of Taylor–Dean flows from Taylor–Couette flow to Dean flow were also measured at sub-critical conditions. Typical results are shown in figure 20 for various ratios of the pressure gradient to the shear driving force. The solid curves are again the predictions of the Oldroyd-B model, which gives base flows which are identical to those of a Newtonian fluid. The error bars in figure 20 again indicate the errors in the mean determined from a time series measurement taken at various points along the gap. The error between the predictions and the experiments are within 5.0% of the maximum velocity of the flow. It is not known at this time whether this 5% error is due to deficiencies in the Oldroyd-B model or lingering effects of the flow block. However, we believe this agreement is generally good and further experimental studies aimed at improving the accuracy of the LDV measurements are underway.

5.2. *Flow visualizations*

Flow visualization experiments were performed to determine the nature of the flow at the transition. A typical series of results of flow visualization and spectral image analysis for the elastic Dean flow instability is shown in figures 21–22. At a Deborah number of approximately 33, the velocity field for Dean flow undergoes a transition from the steady, purely azimuthal flow to secondary vortex flow. Figure 21(*a*) is the digitized image of Dean flow near the onset of the instability, which shows the

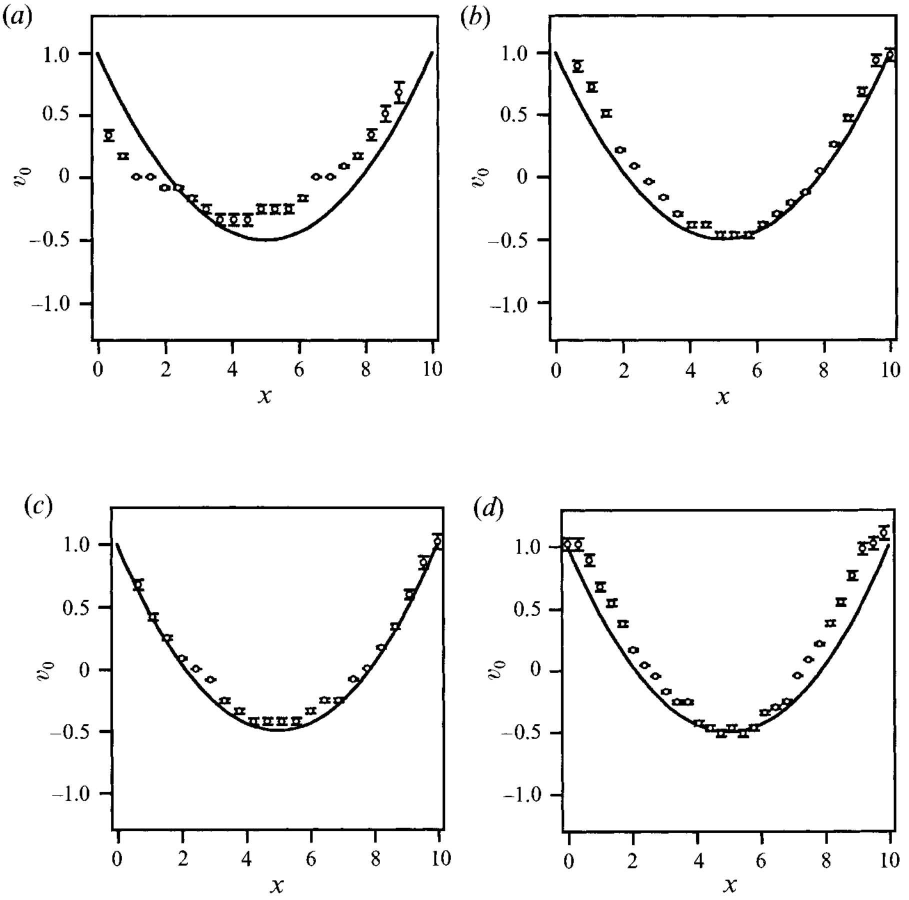

FIGURE 19. The base state azimuthal velocity *vs.* radial position in Dean flow at various azimuthal angles (*a*) $\theta = 15°$, (*b*) $\theta = 45°$, (*c*) $\theta = 90°$, (*d*) $\theta = 270°$. The symbols are data obtained from LDV measurements, and the lines are the predictions of the Oldroyd-B model. The error bars indicate the errors in the mean determined from a time series measurement taken at various points along the gap.

development of evenly spaced, banded vortex structures. These elastic vortices evolve into finer cells as time progresses (see figure 21 *b*). A similar time evolution of the elastic vortices has been observed in studies of the elastic instabilities in Taylor–Couette flow. These observations include studies by Larson *et al.* (1990) and Shaqfeh *et al.* (1992). It is important to note that the linear stability theory predicts a very shallow minimum in the plot of the critical Deborah number versus α for both flows (see figure 2). Thus, above the critical condition, we might expect a range of wavenumbers to become unstable, and a multiple wavelength pattern may thus emerge. Note that in a later publication, we shall examine the nonlinear effects on these elastic vortices as well as the interaction of unstable modes and their harmonics (Joo & Shaqfeh 1993).

The intensity profile along the axial direction and the power spectrum of its fast Fourier transform are shown in figure 21 again at the onset of the Dean instability. The intensity profile was obtained by taking one pixel column of the digitized image (figure 21 *a*) and plotting the pixel intensity along the axial coordinate. The intensity was normalized with the maximum number of the gray scale (256 gray scales). The peaks in the intensity profile represent the bright bands, and the minima represent the dark regions. Since plate-like mica flakes reflect light depending on their orientation, the

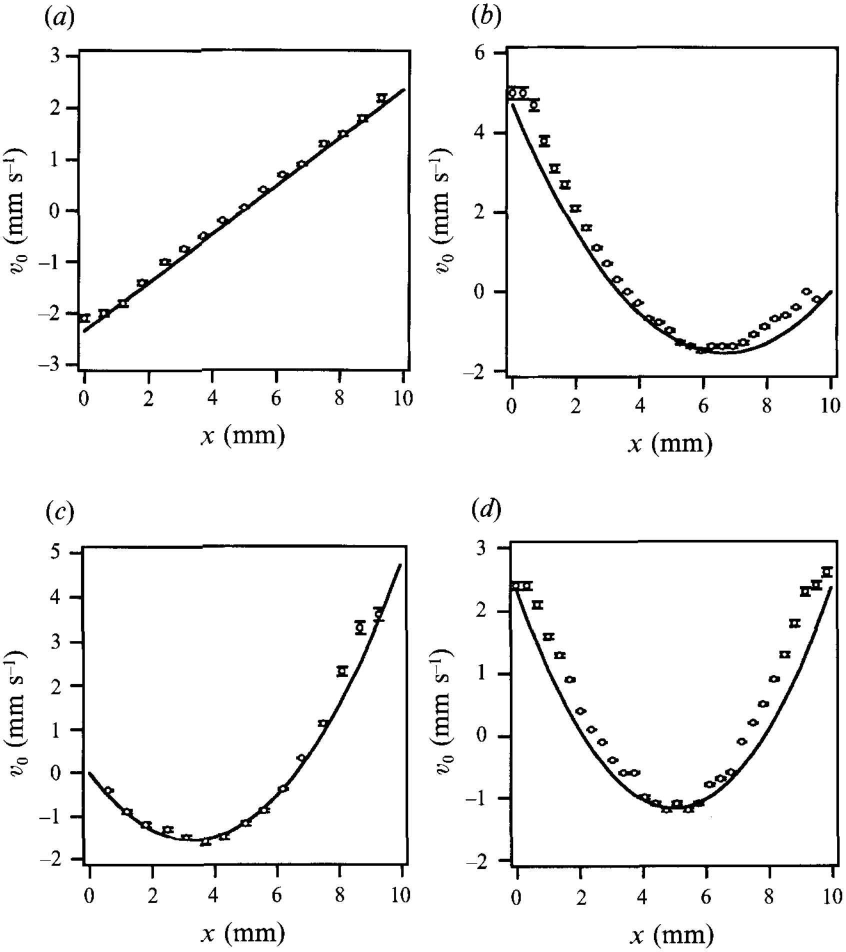

FIGURE 20. The base state azimuthal velocity *vs.* radial position in Taylor–Dean flows (*a*) $\delta = 0$ (Taylor–Couette flow), (*b*) $\delta^* = 0.75$, (*c*) $\delta = 0.75$, (*d*) $\delta = 1$ (Dean flow). The symbols are data obtained from LDV measurements, and the lines are the predictions of the Oldroyd-B model. The error bars indicate the errors in the mean determined from a time series measurement taken at various points along the gap.

dark region represents the area in which the mica flakes are oriented perpendicular to the outer cylinder, while a bright region indicates that they are oriented parallel to the outer cylinder. Thus, two vortices are formed between two dark bands. The critical wavenumber obtained from this spectral image analysis is in good agreement with the theoretical value shown in the figure.

In a similar manner, we obtain the critical wavenumber and the critical Deborah number for a host of Taylor–Dean flows created by varying the ratios of the pressure gradient to the shearing driving force by changing the relative cylinder rotation speed. In figure 23, we have plotted both experimental and theoretical values of the critical Deborah number and the critical wavenumber for all

$$0 \leqslant \delta = (3\Omega_1 + 3\Omega_2)/(2\Omega_1 + 4\Omega_2) \leqslant 1,$$

when the shear rate due to the cylinder rotation is positive ($\beta > 0$). It should be noted that we have plotted predictions for the most unstable mode, whether it is

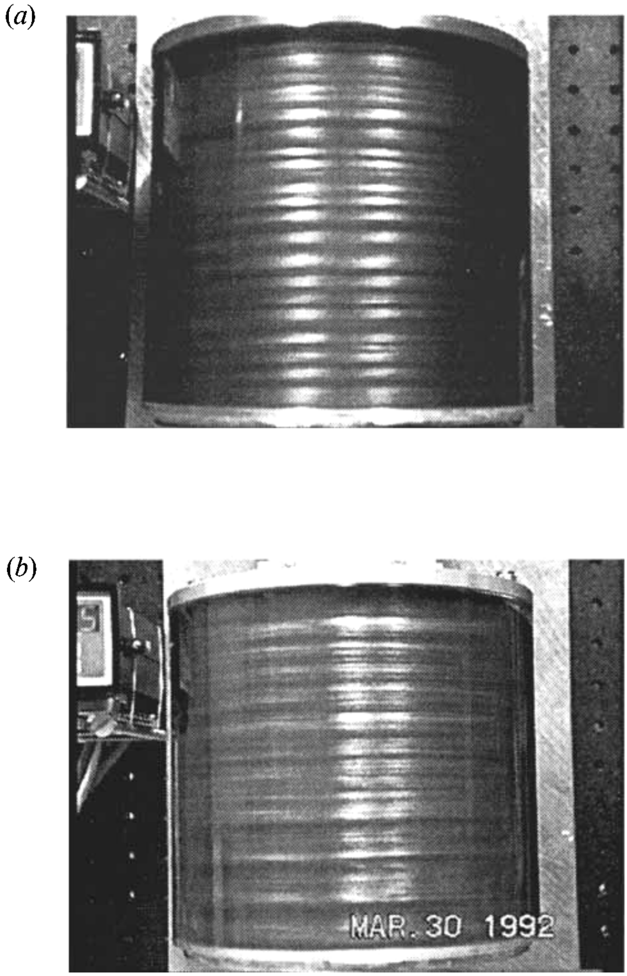

FIGURE 21. Flow visualizations in Dean flow (*a*) shortly after the onset of the secondary flow, and (*b*) after later development.

oscillatory or stationary, or whether it is axisymmetric or non-axisymmetric. As previously presented, there is a purely elastic instability in Dean flow ($\delta = 1$) which is a stationary, axisymmetric mode, while there is an oscillatory, non-axisymmetric instability in Taylor–Couette flow ($\delta = 0$). Both experimental and theoretical values of the critical Deborah number monotonicially increase, as δ is increased from $\delta = 0$ to $\delta = 1$ (see figure 23*a*). However, the experimental values from flow visualizations are higher than the theoretical predictions. It should be noted that critical conditions were always at shear rates within apparent Oldroyd-B behaviour (cf. figure 23*a*). The critical wavenumber is predicted to remain almost constant, while the critical wavenumber obtained from this spectral image analysis increases slightly and then decreases, as δ increased (see figure 23*b*).

When the shear rate due to the cylinder rotation is negative ($\beta < 0$), the stability characteristics are found to be significantly different from those when it is positive ($\beta > 0$). Both experimental and theoretical values of the critical Deborah number and the critical wavenumber for all $0 \leqslant \delta^* = (3\Omega_1 + 3\Omega_2)/(4\Omega_1 + 2\Omega_2) \leqslant 1$ are shown in

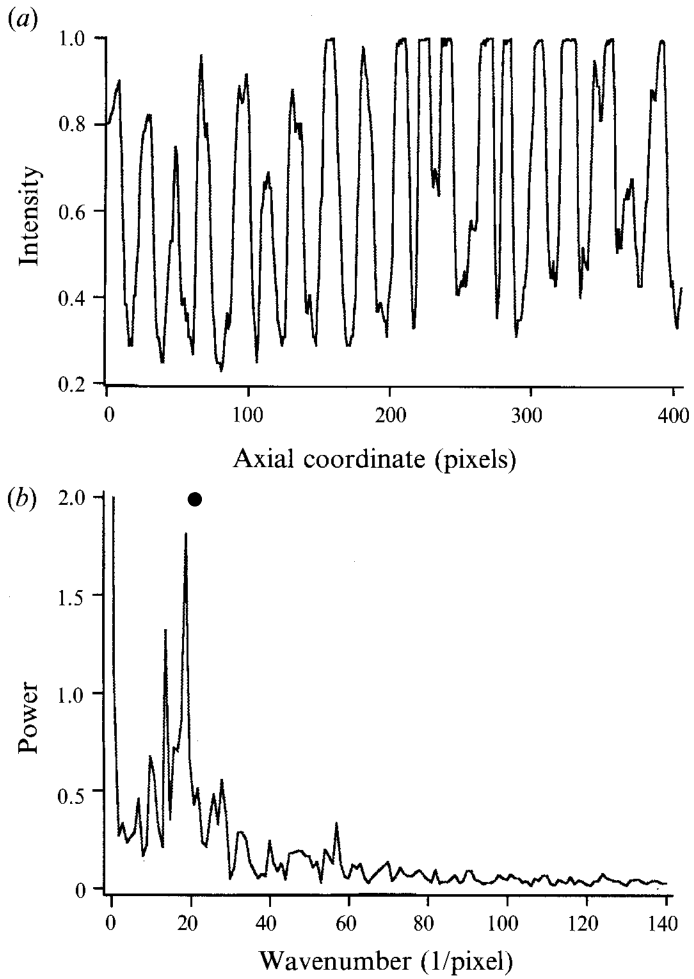

FIGURE 22. Image analysis for at the onset of the Dean flow instability (*a*) intensity profiles along the axial coordinate, (*b*) the fast Fourier transform of the intensity profile. ●, critical wavenumber for Dean flow from the linear stability analysis.

figure 24. The limiting cases, $\delta^* = 0$ and $\delta^* = 1$ correspond to Taylor–Couette flow and Dean flow, respectively. When an azimuthal pressure gradient is added to Taylor–Couette flow, it increases both theoretical and measured critical Deborah number while also increasing the critical wavenumber (see figure 23*a*). Moreover, adding shearing due to cylinder rotation to Dean flow also increases both the experimental and the theoretical values of the critical Deborah number and the critical wavenumber. When δ^* is near 0.4–0.6, the eigenvalue problem was found to be very stiff owing to the large values of the wavenumber and the Deborah number near the stability boundary, and for obtaining precise values of the critical conditions, one must either use an alternative numerical method or employ a large wavenumber analysis. In the same region, experimental data show no evidence of the flow instability throughout the range of Deborah number investigated.

Although there is a quantitative discrepancy between data and theory, the qualitative trends in the data are in agreement with our theoretical predictions. One might not expect quantitative agreement when one notes that only periodic disturbances in the azimuthal direction are considered in the linear stability analysis in §2 while in the

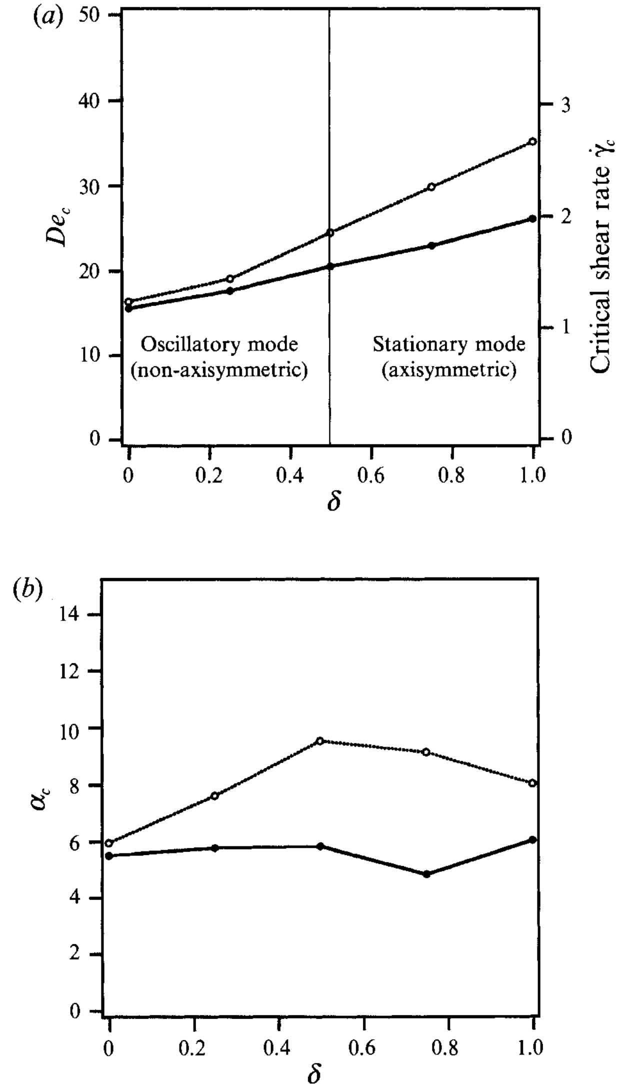

FIGURE 23. Comparison between experimental data and theoretical predictions when the velocity gradient due to the shearing by the cylinder rotation is positive ($\beta > 0$) (*a*) De_c *vs.* δ, and (*b*) α_c *vs.* δ. —●—, theoretical prediction, ···○···, data from the flow-visualization experiments. Note that corresponding critical shear rates ($\dot{\gamma}_c = De_c/\lambda$) are shown on the right-hand axis.

experiments the disturbances are not periodic in the azimuthal direction owing to the existence of the block. In addition, the fluid used is characterized by a spectrum of timescales rather than a single relaxation time (cf. figure 15). Finally, it should be noted that, although we did observe a non-axisymmetric vortex flow in some flow-visualization experiments in the range $\delta < 0.5$ (see Joo 1993), it was difficult to analyse owing to the time evolution of the vortices into finer cells. The equally-banded vortex structures were not found to be stabilized for all flows throughout the range investigated. They lasted less than a few seconds, and then evolved into finer structures over several hundreds seconds. This is very similar to the nonlinear development reported by Larson *et al.* (1990), and no explanation for this nonlinear development is available at this time.

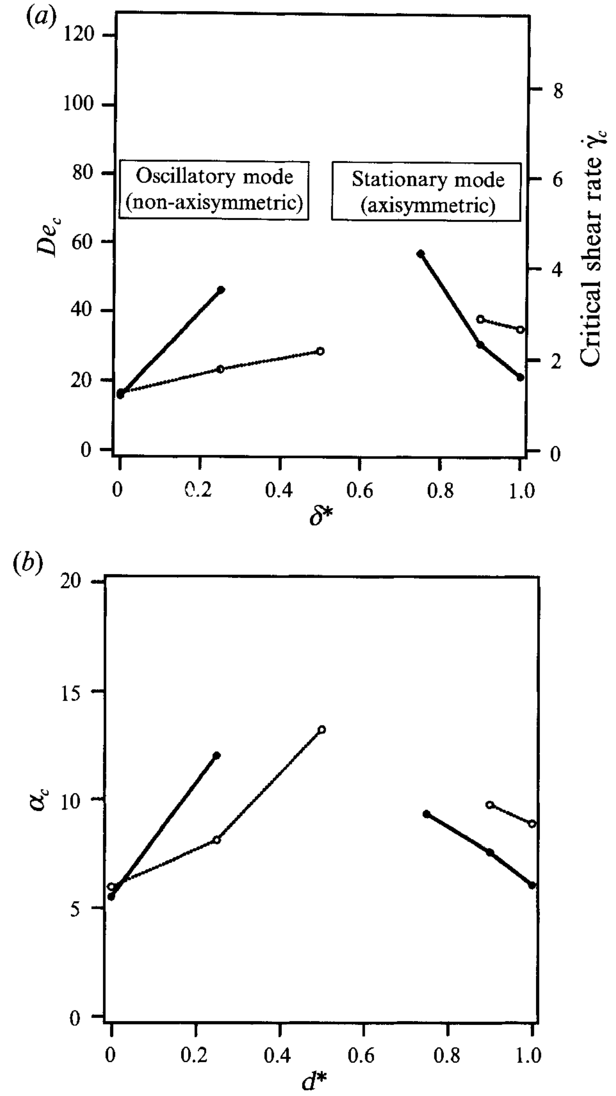

FIGURE 24. Comparison between experimental data and theoretical predictions when the velocity gradient due to the shearing by the cylinder rotation is negative ($\beta < 0$) (*a*) De_c *vs.* δ^*, and (*b*) α_c *vs.* δ^*. —●—, theoretical prediction, ···○···, data from the flow-visualization experiments. Note that corresponding critical shear rates ($\dot{\gamma}_c = De_c/\lambda$) are shown on the right-hand axis.

5.3. *Time dependent LDV measurements of the axial velocity*

Laser-Doppler velocimetry was employed to determine the frequency of the oscillation of the disturbances after flow transition. When the velocity undergoes the transition from steady, purely azimuthal flow to a secondary vortex flow, both new axial and radial components of the velocity develop. The axial velocity at a fixed position ($x = \frac{2}{3}$) was measured as a function of time using LDV. The linear stability results predict that the non-axisymmetric, oscillatory mode is more unstable than the axisymmetric one when the shearing by the cylinder rotation is the dominant flow-driving force, while the axisymmetric, stationary mode is more unstable when the pressure gradient becomes dominant. Experimentally, it was difficult to make measurements of time-dependent flows near De_{cr} with good accuracy, because the

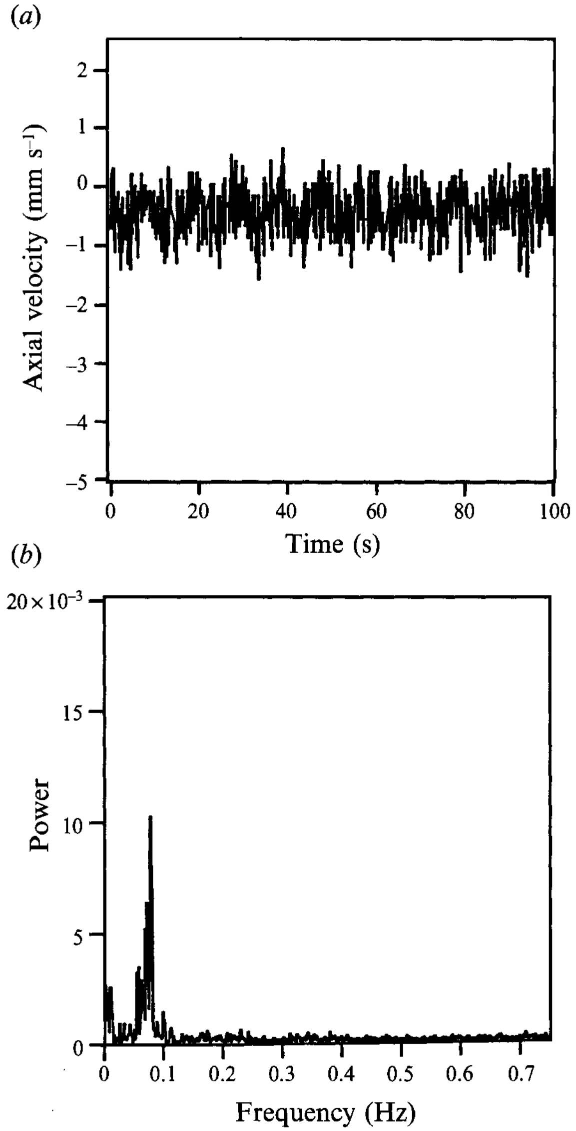

FIGURE 25. (*a*) A time-dependent measurement of the axial velocity at $De = 31$ when only the inner cylinder drives Taylor–Couette flow ($\beta = -1$), and (*b*) its FFT.

amplitude of the oscillation was very low. Thus, throughout the following time dependent measurements of the axial velocity, the data were obtained at a Deborah number which was from 25% to 65% above the critical values predicted by the theory in each case. This 25% to 65% above the critical is high, but signal to noise in the amplitude measurements requires it, and we do not know whether the linear stability predictions are good under these supercritical conditions. For the same reason, another well-characterized PIB/PB Boger fluid with a lower relaxation time $\lambda = 7$ s was used (thus increasing the flow velocity at the critical conditions), and the rheological behaviour of this fluid can be found elsewhere (Joo 1993).

First, the axial velocity in two Taylor–Couette flows with different values of β was measured at $De = 31$ which was 65% above the critical. Figure 24 presents the time-

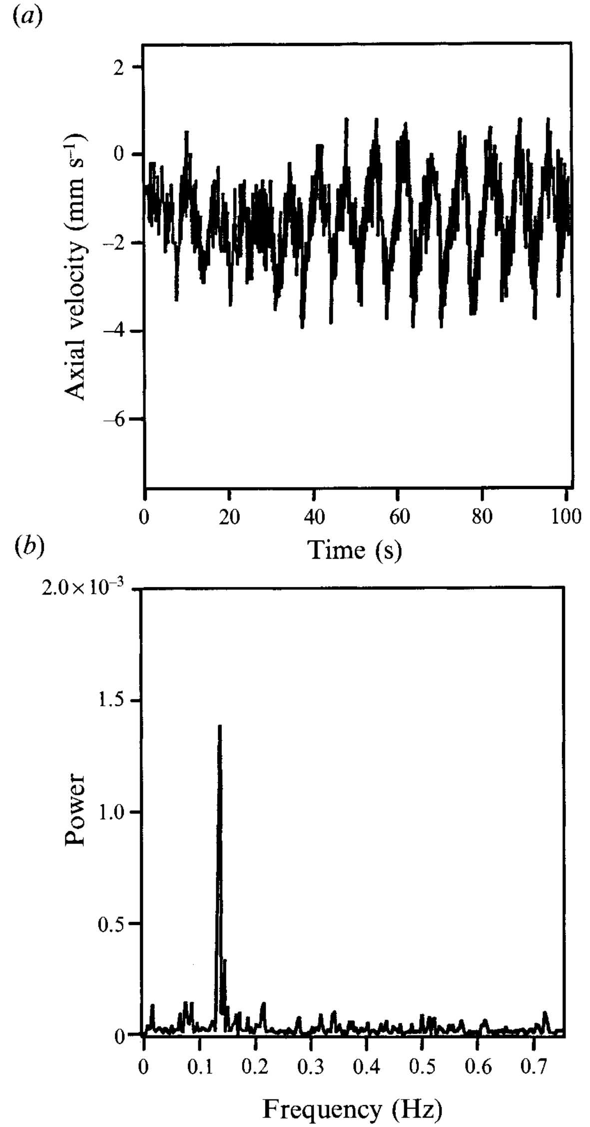

FIGURE 26. (*a*) A time-dependent measurement of the axial velocity at $De = 31$ when only the outer cylinder drives Taylor–Couette flow ($\beta = \infty$), and (*b*) its FFT.

dependent measurement of the axial velocity and the power spectrum of its fast Fourier transform (FFT), when the outer cylinder was held stationary with the inner one rotating ($\beta = -1$). The axial velocity shows a clear oscillation and the frequency of this oscillation is $f_i = 0.07$ Hz. Although this frequency was measured at a fixed radial position ($x = \frac{2}{3}$), it was also found that the same oscillation, but with different amplitude appears throughout the flow field. The frequency made dimensionless with the polymer relaxation time is $\bar{\omega} = 2\pi\lambda f_i \equiv 3$. Although this value is much larger than the theoretical prediction of the most unstable mode 0.1, it is consistent with the value 3.1 obtained by Muller, Shaqfeh & Larson (1993) under similar experimental conditions. However, it is important to note that under these supercritical conditions, not only the most unstable mode ($n = 1$) but also other modes ($n = 2$, $n = 0$, $n = 3$ and

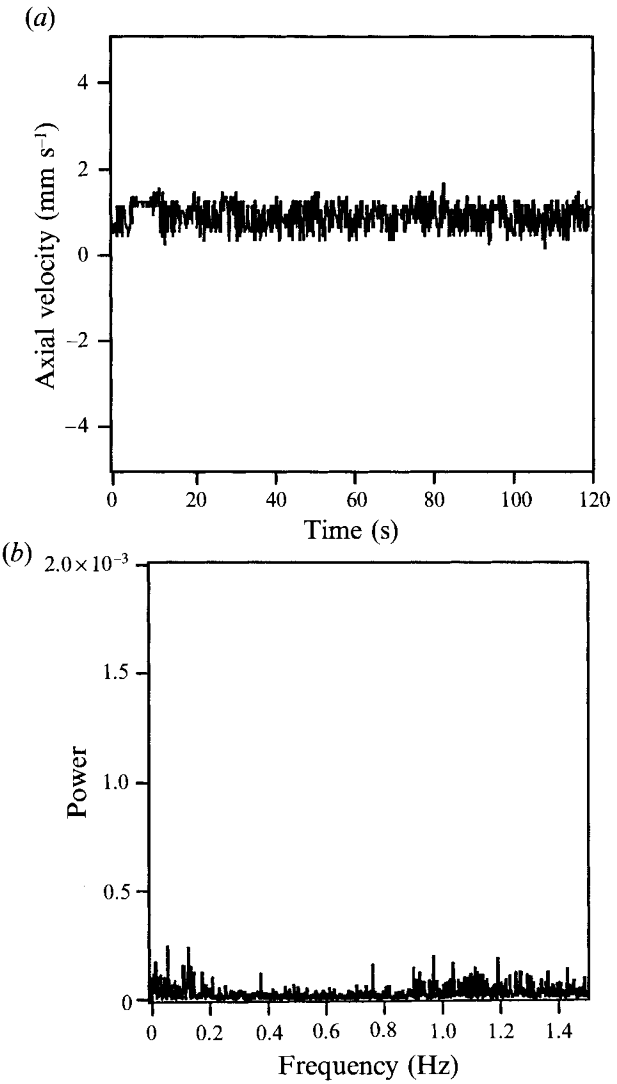

FIGURE 27. (*a*) A time-dependent measurement of the axial velocity for Dean flow at $De = 41$, and (*b*) its FFT.

$n = 4$) are unstable. As shown in table 1, the theoretical predictions of the frequency of oscillation for these modes are 0.632, 0.779, 1.21, and 1.57, respectively, and yet the frequency we obtained from the LDV measurement does not appear to correspond to any of these frequencies. Figure 25 shows the axial velocity and FFT, when Taylor–Couette flow was driven by rotation of the outer cylinder only ($\beta = \infty$). The axial velocity also shows a clear oscillation, but the frequency of this oscillation is $f_0 = 0.13$ which is different from the frequency $f_i = 0.07$ when only the inner cylinder drives Taylor–Couette flow. We note that different frequencies were obtained in two Taylor–Couette flow experiments at different values of β, but at the same value of De (i.e. the rotation speed of the outer cylinder for $\beta = \infty$ was the same as that of the inner cylinder for $\beta = -1$). The dimensionless frequency $\bar{\omega}$ is about 5.7 which is, again, larger than the theoretical prediction of the most unstable mode (1.97). However, again a number of modes are unstable at these conditions and the theoretical predictions of the

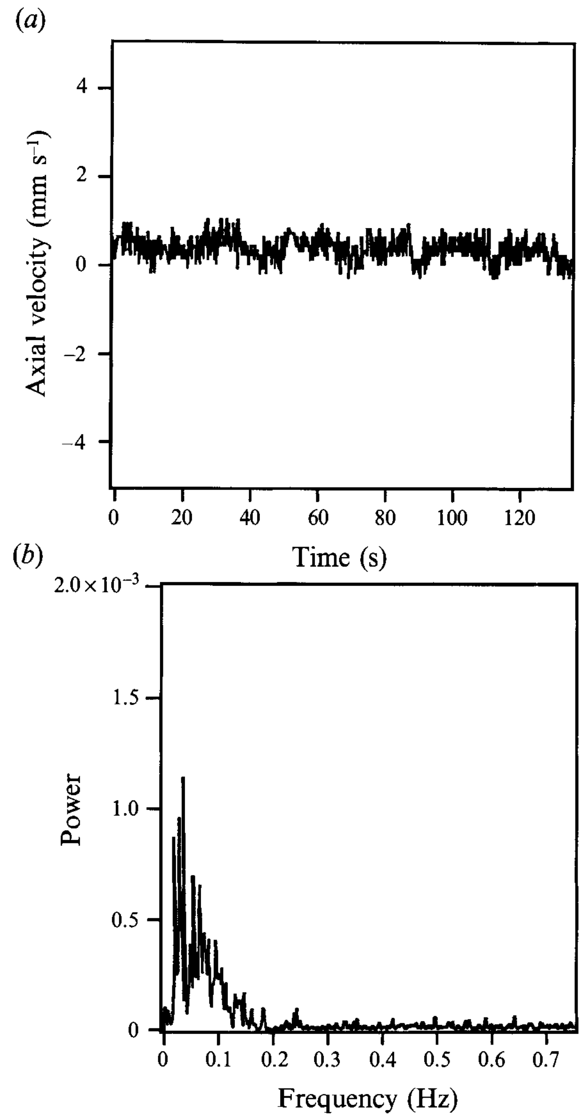

FIGURE 28. (*a*) A time-dependent measurement of the axial velocity for Taylor–Dean flow at $De = 24$ ($\delta = 0.25$), and (*b*) its FFT.

frequency of oscillation for the other unstable modes ($n = 2$, $n = 0$, $n = 3$ and $n = 4$) are 3.753, 0.779, 6.89 and 12.58, respectively. If we insert the frequencies from two Taylor–Couette flow experiments in (18), the azimuthal wavenumber n can be determined. Our linear stability analysis predicts that the non-axisymmetric mode with $n = 1$ is the most unstable mode, while the azimuthal wavenumber from (18) $n \approx 2$. Despite the inability of linear analysis to predict the frequency precisely under these supercritical conditions, the difference in the frequency of oscillation between the two Taylor–Couette flow experiments at different values of β suggests that the instability in Taylor–Couette flow may be a non-axisymmetric mode.

The axial velocity in Dean flow at $De = 41$, which was 25% above the critical, is shown in figure 26(*a*), and it does not appear to show a time-dependent behaviour. The corresponding FFT shown in figure 26(*b*) also indicates that the purely elastic

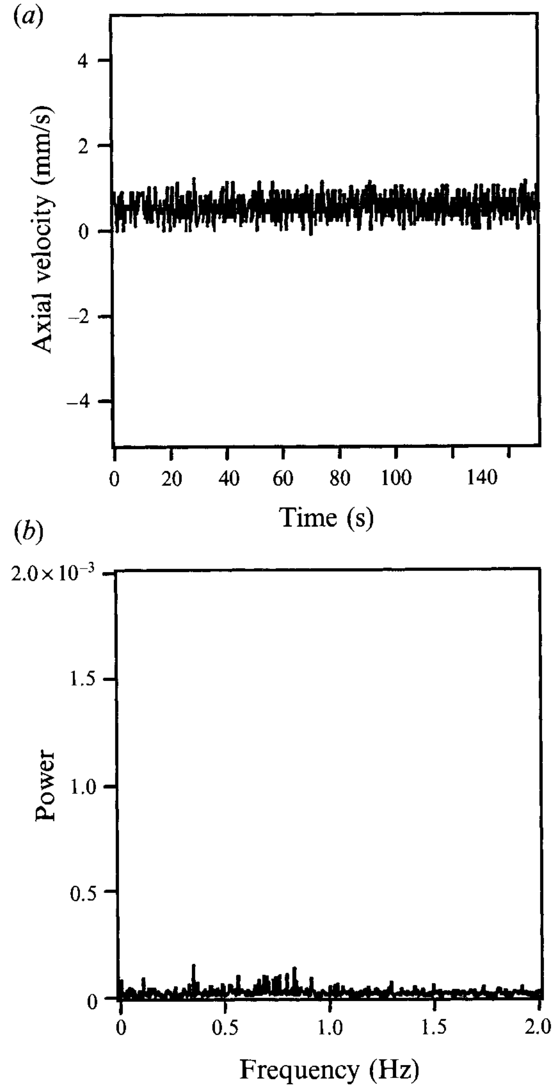

FIGURE 29. (*a*) A long dependent measurement of the axial velocity for Taylor–Dean flow at $De = 33$ ($\delta = 0.75$), and (*b*) its FFT.

instability in Dean flow is a stationary mode. In addition, this suggests that the Dean flow instability is the stationary, axisymmetric mode discussed previously, rather than the oscillatory, non-axisymmetric modes.

Figures 27 and 28 present the axial velocity data at a Deborah number which was 25% above the critical in each case and the FFTs for Taylor–Dean flow at two different values of δ. For $\delta = 0.25$, the axial velocity and its FFT show a time-dependent behaviour, and the frequency of the oscillation is $f_{\delta=0.25} = 0.05$ (see figure 27). This result demonstrates that the instability in Taylor–Dean flow is an oscillatory mode, when the shearing by the cylinder rotation is the dominant flow-driving force. On the other hand, when the pressure gradient is dominant ($\delta = 0.75$), the axial velocity and its FFT does not show any oscillation, which suggests that the instability is an axisymmetric, stationary mode.

In summary, our flow-visualization experiments and LDV measurements are consistent with the theoretical predictions that the non-axisymmetric, oscillatory mode is more unstable than the axisymmetric one when the shearing by the cylinder rotation is the dominant flow-driving force, while an axisymmetric, stationary mode is more unstable when the pressure gradient becomes dominant.

6. Summary and conclusion

We have presented theoretical and experimental results that demonstrate the existence of purely elastic instabilities in viscoelastic flows between rotating cylinders with an azimuthal pressure gradient acting around cylinders. First, the linear stability of the Taylor–Dean flow of an Oldroyd-B model fluid with respect to non-axisymmetric disturbances was considered. These results showed that certain non-axisymmetric modes are more unstable than the axisymmetric one when the shearing by the cylinder rotation is the dominant flow-driving force, while the axisymmetric mode is more unstable when the pressure gradient becomes dominant. The structure of the non-axisymmetric vortex flow at the onset of the Taylor–Couette flow instability was also shown. Furthermore, we investigated the mechanism of purely elastic Taylor–Dean instability with respect to non-axisymmetric disturbances through an examination of the disturbance-energy equation. It is found that the mechanism of the elastic Taylor–Dean instability is associated with the coupling between the disturbance polymeric stresses and the base state velocity gradients owing to the azimuthal variation of the disturbance flow. Experimental evidence of non-inertial, cellular instabilities in this Taylor–Dean flow of a well-characterized polyisobutylene/polybutene Boger fluid was then presented. Flow-visualization experiments near the critical conditions show the transition from purely azimuthal flows to secondary vortex flows, and the development of evenly spaced, banded vortex structures. The critical wavenumber obtained from spectral image analysis, and the critical Deborah number are presented for various ratios of the pressure gradient to the shearing driving force. These experimental results were shown to be in good agreement with the theoretical predictions. In addition, laser-Doppler velocimetry (LDV) measurements showed that the instability is a stationary mode when the pressure gradient becomes the dominant flow-driving force, while it is an oscillatory instability when the shearing is dominant. The difference in the frequency of oscillation between the two Taylor–Couette flow experiments at different values of β suggests that the instability in Taylor–Couette flow may be a non-axisymmetric mode. However, the theory is unable to predict the frequency of oscillation witnessed in the experiment. We can suggest no explanation for this discrepancy at this time.

The observation of different relaxation times, and the discrepancy in the comparison of the frequency of the oscillation between our experimental results and the theoretical predictions, however, suggest that the complex dynamics of Taylor–Dean flow may not easily be described by a constitutive model which includes only a single relaxation time, and that any prediction of the complex time-dependent nature of the instability may require a nonlinear analysis.

The authors would like to thank the National Science Foundation for funding this work through a Presidential Young Investigator Award, Grant no. CTS-9057284. In addition, we would like to thank the David and Lucile Packard Foundation for funding, through a fellowship to ESGS.

Appendix. The linear stability equations for non-axisymmetric disturbances in Taylor–Dean flow

In this Appendix, the linear stability equations for non-axisymmetric disturbances in Taylor–Dean flow are given including full finite-gap effects. With Cauchy's equations of motion, the Oldroyd-B constitutive equation, and the boundary conditions, the velocity distribution describing the basic flow can be written as the sum of two terms: a simple shearing flow due to the cylinder rotation, and a Poiseuille flow due to the azimuthal pressure gradient,

$$v_\theta^0 = \Omega_1 R_1 \left\{ \frac{\xi}{\varepsilon^2} \left[(1+\varepsilon x) \ln [R_1(1+\varepsilon x)] + \frac{((1+\varepsilon x)^2(\beta+1)-1)(1+\varepsilon x)}{[(1+\varepsilon x)^2-1]} + \frac{(1+\varepsilon x)^2 \ln (1+\varepsilon x)}{[(1+\varepsilon x)^2-1](1+\varepsilon x)} \right] + \left[\frac{[(1+\varepsilon x)^2(\beta+1)-1](1+\varepsilon x)}{(1+\varepsilon x)^2-1} - \frac{(1+\varepsilon x)^2 \beta}{[(1+\varepsilon x)^2-1](1+\varepsilon x)} \right] \right\}, \tag{A 1}$$

where $\xi = -(\partial P/\partial\theta)\, d^2/2\eta_t R_1^2 \Omega_1$, $\beta = (\Omega_2 - \Omega_1)/\Omega_1$, and $x = (r-R_1)/(R_2-R_1)$ is the gap variable. For $\beta > 0$, we have the following dimensionless expression of the velocity gradient (made dimensionless with the product of the gap d and the shear rate at the outer cylinder):

$$v' = v_\theta^0 - \frac{\varepsilon v_\theta^0}{1+\varepsilon x} = \frac{\bar{\delta}}{(1+\varepsilon x)^2} \left[1 - \frac{(1-(1+\varepsilon x)^2)(1-(1+\varepsilon)^2)}{2(1+\varepsilon)^2 \ln (1+\varepsilon) - \varepsilon(2+\varepsilon)} \right] + \frac{1-\bar{\delta}}{(1+\varepsilon x)^2}, \tag{A 2}$$

where $\bar{\delta} = \bar{\xi}/(\bar{\xi}+\bar{\beta})$. In the narrow-gap limit $\varepsilon \ll 1$, the relative importance of the pressure gradient to the cylinder rotation as flow driving force,

$$\bar{\xi} = \frac{\xi}{\varepsilon} \left(\frac{2(1+\varepsilon x)^2 \ln (1+\varepsilon)}{(1+\varepsilon x)^2 - 1} - 1 \right),$$

and the dimensionless relative rotation rate $\bar{\beta} = 2(1+\varepsilon)^2/2+\varepsilon\beta$ become ξ and β, respectively. Thus, $\bar{\delta}$ becomes δ (cf. (2)) in the narrow-gap limit.

For $\beta < 0$, we have a similar expression for the velocity gradient (made dimensionless with the product of the gap d and the shear rate at the inner cylinder):

$$v' = v_\theta^0 - \frac{\varepsilon v_\theta^0}{1+\varepsilon x} = \frac{\bar{\delta}^*}{(1+\varepsilon x)^2} \left[1 - \frac{(1-(1+\varepsilon x)^2)(1-(1+\varepsilon)^2)}{2(1+\varepsilon)^2 \ln (1+\varepsilon) - \varepsilon(2+\varepsilon)} \right] + \frac{\bar{\delta}^* - 1}{(1+\varepsilon x)^2}, \tag{A 3}$$

where $\bar{\delta}^* = \bar{\xi}/(\bar{\xi}-\bar{\beta})$. Again, $\bar{\delta}^*$ becomes δ^* (cf. (3)) in the narrow-gap limit.

The final stability problem governing small non-axisymmetric disturbances for the Taylor–Dean flow of an Oldroyd-B fluid becomes:

$$V'' - \alpha^2 V = a_1 U''' + a_2 U'' + a_3 U' + a_4 U + a_5 V'' + a_6 V' + a_7 V, \tag{A 4}$$

$$U'''' - 2\alpha^2 U'' + \alpha^4 U = b_1 U''' + b_2 U'' + b_3 U' + b_4 U + b_5 V''' + b_6 V'' + b_7 V' + b_8 V, \tag{A 5}$$

$$V = U = U' = 0 \quad \text{at} \quad x = 0, \quad x = 1, \tag{A 6}$$

$$a_1 = \frac{in\varepsilon}{\alpha^2(1+\varepsilon x)}, \tag{A 7}$$

$$a_2 = \frac{2in\varepsilon^2}{\alpha^2(1+\varepsilon x)^2} - \frac{De\,\mathscr{D}}{S+\mathscr{D}(1-S)}\left(\mathscr{D}+\frac{2n^2\varepsilon^2}{(1+\varepsilon x)^2}\right)v', \tag{A 8}$$

$$\begin{aligned} a_3 = {} & -\frac{in\varepsilon}{(1+\varepsilon x)}\left(1+\frac{2\varepsilon^2}{\alpha^2(1+\varepsilon x)^2}\right) - \frac{De\,\mathscr{D}}{S+\mathscr{D}(1-S)}\times\biggl[2\mathscr{D}v''+(2+\mathscr{D})\frac{\varepsilon v'}{1+\varepsilon x} \\ & + \frac{2in\,De\,\varepsilon v'^2}{1+\varepsilon x}\left(\mathscr{D}+\frac{n^2(\mathscr{D}+1)\,\varepsilon^2}{(1+\varepsilon x)^2}\right)+\frac{n^2\varepsilon^2}{\alpha^2(1+\varepsilon x)^2}\left(v''+\frac{\varepsilon v'}{1+\varepsilon x}\right)\biggr], \end{aligned} \tag{A 9}$$

$$\begin{aligned} a_4 = {} & -\frac{in\varepsilon^2}{(1+\varepsilon x)^2}\left(2+\frac{\varepsilon^2}{\alpha^2(1+\varepsilon x)^2}\right) - \frac{De\,\mathscr{D}}{S+\mathscr{D}(1-S)}\biggl\{-v'''+(1+\mathscr{D})\frac{\varepsilon^2 v'}{(1+\varepsilon x)^2}-\mathscr{D}\alpha^2 v' \\ & + \frac{in\,De\,\varepsilon v'}{1+\varepsilon x}\left(3\mathscr{D}v''+2(2-\mathscr{D})\frac{\varepsilon v'}{1+\varepsilon x}-\frac{2n^2(\mathscr{D}+1)\,\varepsilon^3 v'}{\alpha^2(1+\varepsilon x)^2}\right) \\ & + \frac{n^2\varepsilon^2}{(1+\varepsilon x)^2}\biggl[(2De^2\,\mathscr{D}v'^2+\mathscr{D}+2)\,v'^2+\frac{\varepsilon}{\alpha^2(1+\varepsilon x)}\bigl(v''-(2+\mathscr{D})\frac{\varepsilon v'}{1+\varepsilon x}\biggr]\biggr\}, \end{aligned} \tag{A 10}$$

$$a_5 = -\frac{n^2\varepsilon^2}{(1+\varepsilon x)^2}, \tag{A 11}$$

$$a_6 = -\frac{\varepsilon}{1+\varepsilon x}\left(1-\frac{n^2\varepsilon^2}{(1+\varepsilon x)^2}\right) - \frac{in\,De\,\mathscr{D}\varepsilon v'}{(S+\mathscr{D}(1-S))(1+\varepsilon x)}\left(2\alpha^2+(2-\mathscr{D})\frac{n^2\varepsilon^2}{(1+\varepsilon x)^2}\right), \tag{A 12}$$

$$\begin{aligned} a_7 = {} & \frac{\varepsilon^2}{(1+\varepsilon x)^2}(1+n^2) - \frac{De\,\mathscr{D}}{S+\mathscr{D}(1-S)}\biggl\{\frac{2n^2\,De^2\,\varepsilon^2 v'^2}{(1+\varepsilon x)^2}\left(1+(\mathscr{D}+1)\frac{\varepsilon^2}{\alpha^2(1+\varepsilon x)}\right) \\ & + \frac{in\varepsilon}{1+\varepsilon x}\left[v''-\mathscr{D}(\mathscr{D}+1)\frac{\varepsilon v'}{1+\varepsilon x}+\frac{\varepsilon^2}{\alpha^2(1+\varepsilon x)}\left(v''-\frac{3\varepsilon v'}{1+\varepsilon x}\right)\right]\biggr\}, \end{aligned} \tag{A 13}$$

$$b_1 = -\frac{2\varepsilon}{1+\varepsilon x} - \frac{in\,De\,\mathscr{D}(2-\mathscr{D})\,\varepsilon v'}{(S+\mathscr{D}(1-S))(1+\varepsilon x)}, \tag{A 14}$$

$$\begin{aligned} b_2 = {} & \frac{\varepsilon^2(3+n^2)}{(1+\varepsilon x)^2} - \frac{De\,\mathscr{D}\varepsilon}{(S+\mathscr{D}(1-S))(1+\varepsilon x)} \\ & \times\left[3in\left(v''-\frac{(\mathscr{D}+1)\,\varepsilon v'}{1+\varepsilon x}\right)-\frac{2n^2\,De\,\mathscr{D}(\mathscr{D}+1)\,\varepsilon v'^2}{1+\varepsilon x}\right], \end{aligned} \tag{A 15}$$

$$\begin{aligned} b_3 = {} & \frac{\varepsilon}{1+\varepsilon x}\left(2\alpha^2-\frac{(3+n^2)\,\varepsilon^2}{(1+\varepsilon x)^2}\right) - \frac{in\,De\,\mathscr{D}\varepsilon v'}{(S+\mathscr{D}(1-S))(1+\varepsilon x)}\biggl\{\alpha^2(3\mathscr{D}-4) \\ & + v''' + \frac{\varepsilon v''}{1+\varepsilon x}+\frac{(6\mathscr{D}+1)\,\varepsilon^2 v'}{(1+\varepsilon x)^2}+\frac{n^2\mathscr{D}\varepsilon^2}{(1+\varepsilon x)^2}(1+De^2(2\mathscr{D}+1)\,v'^2) \\ & - \frac{in\,De\,\varepsilon v'}{1+\varepsilon x}\left[2\alpha^2\mathscr{D}(1+2\mathscr{D})\,v' - \frac{\varepsilon}{1+\varepsilon x}\left((\mathscr{D}+5)\,v''+2(\mathscr{D}^2+2\mathscr{D}-1)\frac{\varepsilon v'}{1+\varepsilon x}\right)\right]\biggr\}, \end{aligned} \tag{A 16}$$

$$\begin{aligned} b_4 = &-\frac{\varepsilon^2}{(1+\varepsilon x)^2}\bigg[\alpha^2(2-n^2)-\frac{\varepsilon^2(3+2n^2)}{(1+\varepsilon x)^2}\bigg] \\ &+\frac{De\,\mathscr{D}}{S+\mathscr{D}(1-S)}\bigg\{\frac{2\alpha^2 De(2+\mathscr{D})\,\varepsilon v'}{1+\varepsilon x}\bigg(v''-\frac{2\varepsilon v'}{1+\varepsilon x}\bigg) \\ &+\frac{in\varepsilon}{1+\varepsilon x}\bigg[\alpha^2\bigg(v''+\frac{(\mathscr{D}-5)\,\varepsilon v'}{1+\varepsilon x}\bigg)+\frac{\varepsilon}{1+\varepsilon x}\bigg(v'''+(\mathscr{D}-3)\,v''+\frac{2(2\mathscr{D}+3)\,\varepsilon^2 v'}{(1+\varepsilon x)^2}\bigg) \\ &+\frac{n^2\mathscr{D}\,De\,\varepsilon^2(1-2De^2(2\mathscr{D}+1))\,v'^3}{(1+\varepsilon x)^2}\bigg]-\frac{n^2 De\,\varepsilon^2 v'}{(1+\varepsilon x)^2}\bigg[\alpha^2(4\mathscr{D}^2+2\mathscr{D}+1)\,v' \\ &-\frac{2\varepsilon}{1+\varepsilon x}\bigg((2\mathscr{D}+1)\,v''-\frac{(2\mathscr{D}^2+2\mathscr{D}-1)\,\varepsilon v'}{1+\varepsilon x}\bigg)\bigg]\bigg\}, \end{aligned} \tag{A 17}$$

$$b_5 = -\frac{in\varepsilon}{1+\varepsilon x}, \tag{A 18}$$

$$b_6 = \frac{2in\varepsilon^2}{(1+\varepsilon x)^2}-\frac{n^2\,De\,\mathscr{D}(\mathscr{D}-2)(1-S)\,\varepsilon^2 v'}{(S+\mathscr{D}(1-S))(1+\varepsilon x)^2} \tag{A 19}$$

$$\begin{aligned} b_7 = &-\frac{in\varepsilon}{1+\varepsilon x}\bigg(\alpha^2+\frac{(m-3)\,\varepsilon^2}{(1+\varepsilon x)^2}\bigg) \\ &-\frac{De\,\mathscr{D}}{S+\mathscr{D}(1-S)}\bigg[\frac{2(1+\mathscr{D})\,\varepsilon v'}{1+\varepsilon x}\bigg(\alpha^2-\frac{in^3\varepsilon^2}{(1+\varepsilon x)^2}\bigg)+n^2\bigg(3v''+\frac{(\mathscr{D}+5)\,\varepsilon v'}{1+\varepsilon x}\bigg)\bigg], \end{aligned} \tag{A 20}$$

$$\begin{aligned} b_8 = &\frac{in\varepsilon^2}{(1+\varepsilon x)^2}\bigg(2\alpha^2+\frac{3(n^2-1)\,\varepsilon^2}{(1+\varepsilon x)^2}\bigg)+\frac{De\,\mathscr{D}}{S+\mathscr{D}(1-S)}\bigg\{\frac{\alpha^2\varepsilon^2 v'[2+\mathscr{D}(2+n^2)]}{(1+\varepsilon x)^2} \\ &-n^2\bigg[v'''+\frac{(\mathscr{D}-6)\,\varepsilon v''}{1+\varepsilon x}-\frac{(3\mathscr{D}-13)\,\varepsilon^2 v'}{(1+\varepsilon x)^2}+n^2\mathscr{D}(3\mathscr{D}+2)\,v'\bigg] \\ &-\frac{in\,De\,\varepsilon^2}{(1+\varepsilon x)^2}\bigg[2\alpha^2 v'^2(\mathscr{D}+2)-\frac{n^2\mathscr{D}\varepsilon}{1+\varepsilon x}\bigg((5\mathscr{D}+4)\,v''-\frac{4(3\mathscr{D}+2)\,\varepsilon v'}{1+\varepsilon x}\bigg)\bigg]\bigg\}. \end{aligned} \tag{A 21}$$

The Deborah number in the equations above is defined as the product of the fluid relaxation time λ and the shear rate at the cylinders:

$$De = \frac{\Omega_1}{\varepsilon}(\bar{\xi}+\bar{\beta})\,\lambda \quad \text{for } \beta > 0, \tag{A 22}$$

$$De = \frac{\Omega_1}{\varepsilon}(\bar{\xi}-\bar{\beta})\,\lambda \quad \text{and for } \beta < 0. \tag{A 23}$$

In addition, the primes refer to derivatives with respect to the gap variable x, and $\mathscr{D} = 1/(1-\mathrm{i}\bar{\omega}+\varepsilon in\,De v_\theta^0)$. In the narrow-gap limit $\varepsilon \ll 1$, the eigenvalue equations (A 4) and (A 5) become (10) and (11).

REFERENCES

BERIS, A. N. & AVGOUSTI, M. 1992 Viscoelastic flow instabilities: inception and non-linear evolution. In *Theoretical and Applied Rheology, Proceedings of the X International Congress on Rheology, Belgium* (ed. P. Modenaers & R. Keunings,) vol. 1, pp. 33–38. Elsevier.

BIRD, R. B., CURTISS, C. F., ARMSTRONG, R. C. & HASSAGER, O. 1987 *Dynamics of Polymeric Liquids*, 2nd edn, vol. 2. Wiley-Interscience.

BOGER, D. V. 1977/1978 A highly elastic constant-viscosity fluid. *J. Non-Newtonian Fluid Mech.* **3**, 87–91.

BREWSTER, D. B. & NISSAN, A. H. 1958 Hydrodynamics of flow between horizontal concentric cylinders. I. Flow due to the rotation of cylinder. *Chem. Engng Sci.* **7**, 215–221.

CHANDRASEKAR, S. 1961 *Hydrodynamic Stability*. Clarendon Press, Oxford.

COLES, D. 1965 Transition in circular Couette flow. *J. Fluid Mech.* **93**, 385–425.

CONTE, S. D. 1966 The numerical solutions of linear boundary value problems. *SIAM Rev.* **8**, 309–321.

DEAN, W. R. 1928 Fluid motion in a curved channel. *Proc. R. Soc. Lond.* A **121**, 402–420.

DIPRIMA, R. C. 1959 The stability of viscous flow between rotating concentric cylinders with a pressure gradient acting around the cylinder. *J. Fluid Mech.* **6**, 462–468.

DIPRIMA, R. C. 1961 Stability of nonrotationally symmetric disturbances for viscous flow between rotating cylinders. *Phys. Fluids* **4**, 751–755.

DIPRIMA, R. C. & SWINNEY, H. L. 1981 Instabilities and transition in flow between concentric rotating cylinders. In *Hydrodynamic Instabilities and the transition to turbulence*, 2nd edn (ed. H. L. Swinney & J. P. Gollub), pp. 139–180. Springer.

DRAZIN, P. G. & REID, W. H. 1981 *Hydrodynamic Stability*. Cambridge University Press.

GUPTA, R. K., SRIDHAR, T. & RYAN, M. E. 1983 Model viscoelastic liquids. *J. Non-Newtonian Fluid Mech.* **12**, 233–241.

JOO, Y. L. 1993 A theoretical and experimental investigation of vis·oelastic instabilities in Taylor–Dean flow. PhD thesis, Stanford University.

JOO, Y. L. & SHAQFEH, E. S. G. 1991 Viscoelastic Poiseuille flow through a curved channel: a new elastic instability. *Phys. Fluids* A **3**, 1691–1694.

JOO, Y. L. & SHAQFEH, E. S. G. 1992 A purely elastic instability in Dean and Taylor–Dean flow. *Phys. Fluids* A **4**, 524–543.

JOO, Y. L. & SHAQFEH, E. S. G. 1993 Weakly nonlinear analysis and experimental studies in the viscoelastic Taylor–Dean instability. In preparation.

KELLER, H. B. 1961 *Numerical Methods for Two-Point Boundary-Value Problems*. Cinn-Blaisdell, Waltham, MA.

LARSON, R. G., SHAQFEH, E. S. G. & MULLER, S. J. 1990 A purely elastic instability in Taylor–Couette flow. *J. Fluid Mech.* **218**, 573–600.

MACKAY, M. E. & BOGER, D. V. 1987 An explanation of the rheological properties of Boger fluids. *J. Non-Newtonian Fluid Mech.* **22**, 235–243.

MCKINLEY, G. H., BYARS, J. A. & BROWN, R. A. 1991*a* Observations on the elastic instability in cone-and-plate and parallel-plate flows of a polyisobutylene Boger fluid. *J. Non-Newtonian Fluid Mech.* **40**, 201–229.

MCKINLEY, G. H., RAIFORD, W. P., BROWN, R. A. & ARMSTRONG, R. C. 1991*b* Nonlinear dynamics of viscoelastic flow in axisymmetric abrupt contractions. *J. Fluid Mech.* **223**, 411–56.

MAGDA, J. J. & LARSON, R. G. 1988 A transition in ideal liquids during the shear flow. *J. Non-Newtonian Fluid Mech.* **30**, 1–19.

MULLER, S. J., SHAQFEH, E. S. G. & LARSON, R. G. 1993 Experimental studies of the onset of oscillatory instability in viscoelastic Taylor–Couette flow. *J. Non-Newtonian Fluid Mech.* **46**, 315–330.

MUTABAZI, I., NORMAND, C., PEERHOSSAINI, H. & WESFREID, J. E. 1989 Oscillatory modes in the flow between two horizontal corotating cylinders with a partially filled gap. *Phys. Rev.* A **39**, 763–771.

MUTABAZI, I., HEGSETH, J. J. & ANDERECK, C. D. 1990 Spatiotemporal pattern modulations in the Taylor–Dean system. *Phys. Rev. Lett.* **64**, 1729–1732.

PHAN-THIEN, N. 1983 Coaxial-disk flow of an Oldroyd-B fluid: exact solution and stability. *J. Non-Newtonian Fluid Mech.* **13**, 325–340.

PHAN-THIEN, N. 1985 Cone-and-plate flow of an Oldroyd-B fluid is unstable. *J. Non-Newtonian Fluid Mech.* **17**, 37–44.

QUINZANI, L. M., MCKINLEY, G. H., BROWN, R. A. & ARMSTRONG, R. C. 1991 Modeling the rheology of polyisobutylene solutions. *J. Rheol.* **34**, 705.

RANEY, D. C. & CHANG, T. S. 1971 Oscillatory modes of instability for flow between rotating cylinders with a transverse pressure gradient. *Z. angew. Math. Phys.* **22**, 680–690.

SHAQFEH, E. S. G. & ACRIVOS, A. 1987 The effects of inertia on the stability of convective flow in inclined particle settlers. *Phys. Fluids* **30**, 960–973.

SHAQFEH, E. S. G., MULLER, S. J. & LARSON, R. G. 1992 The effects of gap width and dilute solution properties on the viscoelastic Taylor–Couette instability. *J. Fluid Mech.* **235**, 285–317.

TAYLOR, G. I. 1923 Stability of a viscous liquid contained between two rotating cylinders. *Phil. Trans. R. Soc. Lond.* A **223**, 289–343.